This article was downloaded by: [National Chiao Tung University]
On: 21 November 2012, At: 06:29
Publisher: Taylor & Francis
Informa Ltd Registered in England and Wales Registered Number: 1072954 Registered office: Mortimer House, 37-41 Mortimer Street, London W1T 3JH, UK

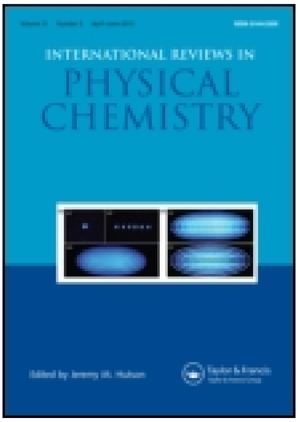

International Reviews in Physical Chemistry

Publication details, including instructions for authors and subscription information:
http://www.tandfonline.com/loi/trpc20

Characterisation of electron transport and charge recombination using temporally resolved and frequency-domain techniques for dye-sensitised solar cells

Lu-Lin Li [a], Yu-Cheng Chang [a], Hui-Ping Wu [a] & Eric Wei-Guang Diau [a]

[a] Department of Applied Chemistry and Institute of Molecular Science, National Chiao Tung University, Hsinchu 30010, Taiwan (ROC)

Version of record first published: 31 Oct 2012.

To cite this article: Lu-Lin Li , Yu-Cheng Chang , Hui-Ping Wu & Eric Wei-Guang Diau (2012): Characterisation of electron transport and charge recombination using temporally resolved and frequency-domain techniques for dye-sensitised solar cells, International Reviews in Physical Chemistry, 31:3, 420-467

To link to this article: http://dx.doi.org/10.1080/0144235X.2012.733539

PLEASE SCROLL DOWN FOR ARTICLE

Full terms and conditions of use: http://www.tandfonline.com/page/terms-and-conditions

This article may be used for research, teaching, and private study purposes. Any substantial or systematic reproduction, redistribution, reselling, loan, sub-licensing, systematic supply, or distribution in any form to anyone is expressly forbidden.

The publisher does not give any warranty express or implied or make any representation that the contents will be complete or accurate or up to date. The accuracy of any instructions, formulae, and drug doses should be independently verified with primary sources. The publisher shall not be liable for any loss, actions, claims, proceedings, demand, or costs or damages whatsoever or howsoever caused arising directly or indirectly in connection with or arising out of the use of this material.

Downloaded by [National Chiao Tung University] at 06:29 21 November 2012

International Reviews in Physical Chemistry
Vol. 31, No. 3, July–September 2012, 420–467

Downloaded by [National Chiao Tung University] at 06:29 21 November 2012

Characterisation of electron transport and charge recombination using temporally resolved and frequency-domain techniques for dye-sensitised solar cells

Lu-Lin Li, Yu-Cheng Chang, Hui-Ping Wu and Eric Wei-Guang Diau*

Department of Applied Chemistry and Institute of Molecular Science,
National Chiao Tung University, Hsinchu 30010, Taiwan (ROC)

(*Received 30 April 2012; final version received 19 September 2012*)

We review systematically the kinetic characterisation of electron transport and charge recombination in dye-sensitised solar cells (DSSC) using both temporally resolved and frequency-domain techniques. For the temporally resolved approach, charge extraction (CE), transient-photocurrent decay (TCD) and transient-photovoltage decay (TVD) methods are introduced in detail; for the frequency-domain approach, techniques involving electrochemical impedance spectroscopy (EIS), intensity-modulated photocurrent spectroscopy (IMPS) and intensity-modulated photovoltage spectroscopy (IMVS) are presented in detail. The TCD and TVD data are obtained under short-circuit and open-circuit conditions, respectively, and the electron diffusion coefficients and electron lifetimes are extracted from fitting the decay curves accordingly; the IMPS/IMVS results are the counterparts of the TCD/TVD results in the frequency domain. Even though the EIS results are readily acquired, an accurate interpretation of the data requires an appropriate model to determine the internal features of the device. This review provides an account of each technique about its operating principle, experimental setup and data analysis. As case studies for each technique, examples are given to rationalise the observed potential shift, decay coefficients of electron transport and of charge recombination in relation to the corresponding photovoltaic performance of the device.

Keywords: dye-sensitised solar cells; transient photoelectric decays; charge extraction; impedance spectroscopy; TCD; TVD; EIS; IMPS; IMVS

Contents

---

*Corresponding author. Email: diau@mail.nctu.edu.tw

ISSN 0144–235X print/ISSN 1366–591X online
© 2012 Taylor & Francis
http://dx.doi.org/10.1080/0144235X.2012.733539
http://www.tandfonline.com

Downloaded by [National Chiao Tung University] at 06:29 21 November 2012

1. Introduction

Dye-sensitised solar cells (DSSC) are attracting much attention because of their prospective application as the next-generation photovoltaic devices [1–3]. The purpose of such a device is to convert radiant energy into electric energy by establishing an electric potential difference as a basis of an electric current. The intended source of radiant energy is the sun, for which the mean temperature of the sun's surface or solar sphere at 5777 K implies a maximum spectral radiance at 501 nm, corresponding to green light. That radiance decreases rapidly to smaller wavelength, whereas the absorption coefficient of various chemical compounds typically increases rapidly with wavelength toward 200 nm. For the purpose of testing the conversion efficiency, researchers on DSSC use lamps with optical filters to simulate the wavelength distribution of solar radiation. For efficient absorption one must hence select an absorbing chemical compound having strong absorption in the visible and near infrared regions: dyes serve this purpose, and their absorbed radiant energy must be transferred efficiently to other species or materials to generate the potential difference. The objective of research on solar cells is to find an absorbing compound that utilises efficiently the available light and to discover mechanisms to convert efficiently the absorbed energy into an electric potential that can undertake useful work. Figure 1 shows a typical DSSC device; it contains a dye-sensitised mesoporous working electrode (TiO_2, anode) and a counter electrode (Pt-coated, cathode), and has an electrolyte (iodine-based) filling the space between the anode and cathode to serve as a redox mediator in a structure of sandwich type. When the dye molecules absorb sunlight (process 1), electrons are injected into the conduction band of the TiO_2 layer (process 2), which results in a separation of electrons (in the TiO_2 layer) and holes (dye cations); the electrons proceed to the anode (process 3) while the holes are reduced (known as dye regeneration) by the I^- species to produce the I_3^- species (process 4); the I_3^- species are then transported to the cathode at which a catalytic reaction occurs on the surface of the Pt electrode to convert the I_3^- species back to the I^- species (process 5).

These five processes, shown as solid directed lines in Figure 1, are the major elementary operations for a DSSC device in a complete photoelectrochemical cycle to perform external work [3–5]. The performance of a DSSC might become degraded through three competing processes shown as dashed directed lines in Figure 1: (a) rapid non-radiative relaxation due to intramolecular or intermolecular interactions (process 6) to compete with process 2; (b) efficient recombination of charge between electrons in the conduction band (CB) of TiO_2 and the I_3^- species in the electrolyte (process 7) to compete with process 3; (c)

Downloaded by [National Chiao Tung University] at 06:29 21 November 2012

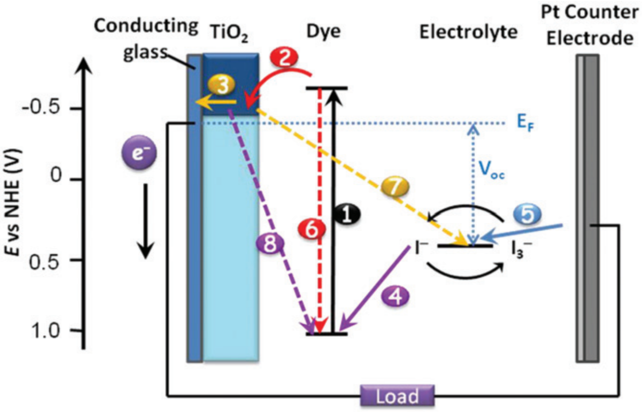

Figure 1. (Colour online) Schematic representation of the operating principle of a DSSC.

rapid electron-hole recombination (process 8) to compete with process 4. For devices made of the most efficient dyes [6–9], processes 2 and 4 are much more rapid than processes 6 and 8, respectively. The key kinetic processes affecting the photovoltaic performance of a device would hence be the competition between processes 3 and 7. In a typical Ru-based DSSC, the time scales for processes 3 and 7 are in the region sub-milliseconds to sub-seconds [5,10,11]; the kinetic ratio of these two processes determines the efficiency of charge collection related to the current output of the device. The voltage output of the device is related to the Fermi level of the TiO_2 potential (V_F), which is determined by the position of the CB potential and the number of electrons at that potential [4,5]. If the injected electrons in the CB of TiO_2 are effectively intercepted by process 7 (charge recombination), the outcome would be to degrade the photocurrent and photovoltage of the device [4,11–13]. To obtain kinetic information about processes 3 and 7, in the present review we provide details of the operating principle and data analysis for a comprehensive understanding of both temporally resolved and frequency-domain techniques, which have been broadly applied for various DSSC systems introduced herein.

Both temporally resolved and frequency-domain techniques are based on a perturbation of small amplitude superimposed on a large bias driving force in the form of either continuous irradiation or an applied dc potential [14]. For the temporally resolved approach, the perturbation probe provides photocurrent or photovoltage decays in the time domain [14–18]; for the frequency-domain approach, it gives the ac potential-induced or modulated light-induced electric response in the frequency domain [14,19–22]. As shown in Figure 2(a) and (b), the kinetic information for processes 3 and 7 are obtainable under two extreme conditions, short circuit and open circuit, respectively. As shown in the figure for a homogeneous light absorption system, the quasi-Fermi level throughout the TiO_2 film is constant at the open-circuit condition (Figure 2b), but at the short-circuit condition a curve shown in Figure 2(a) is used to represent the gradient of the Fermi level across the film and the electrons diffuse directly into the TCO substrate. Under the short-circuit condition, the transport (diffusion) kinetics of the injected electrons in the CB of TiO_2 are monitored through transient photocurrent decay (TCD)

Downloaded by [National Chiao Tung University] at 06:29 21 November 2012

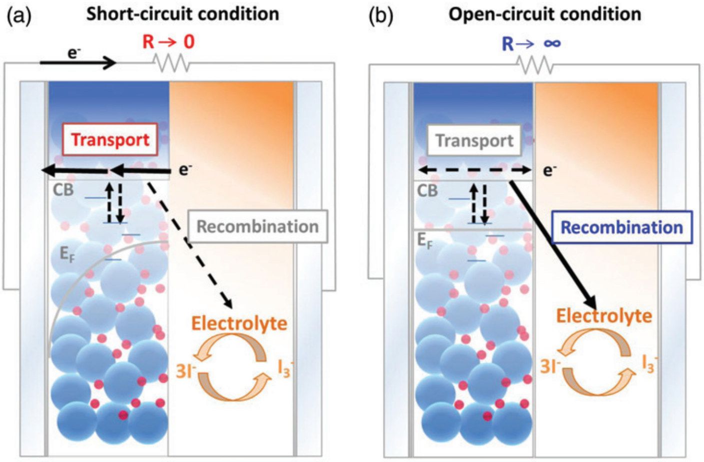

Figure 2. (Colour online) Schematic representations of kinetic processes of a DSSC that are investigated via (a) transient photocurrent decay (TCD) or intensity-modulated photocurrent spectroscopy (IMPS) under short-circuit condition and (b) transient photovoltage decay (TVD) or intensity-modulated photovoltage spectroscopy (IMVS) under open-circuit condition. The solid arrows represent the most probable directions for electron transport and charge recombination at the two extreme conditions. The two-sided arrow shown in (b) represents the electron diffusion at open circuit without a specific direction.

and intensity-modulated photocurrent spectroscopy (IMPS) based on the temporally resolved and frequency-domain approaches, respectively. Under the open-circuit condition, the kinetics of charge recombination (electron interception) are probed via transient photovoltage decay (TVD) and intensity-modulated photovoltage spectroscopy (IMVS) based on the temporally resolved and frequency-domain approaches, respectively. The present review is divided into two parts: the first treats the temporally resolved approach whereas the second discusses the frequency-domain approach. For each part, we introduce the operating principle of the technique, demonstrate the experimental setup and the working principle of the system, perform data analysis to extract the key kinetic information, and provide examples of real systems to consolidate the principle and functionality in relation to the photovoltaic performance of the device. Our objective is to provide an improved understanding of the mechanism of electron transport in specific systems for the purpose of designing or producing new functional materials for DSSC to increase the future performance.

2. Transient photoelectric measurements

2.1. *Principle*

For transient photoelectric measurements, we focus on a system with injected electrons in the CB of TiO_2 after light absorption and electron injection. From an experimental viewpoint, two assumptions are made to simplify our kinetic model [14]: (a) no distinction is made between free and trapped electrons involved in the electron transport (Figure 2a) and charge recombination (Figure 2b) [15]; (b) the recombination of electrons with

Downloaded by [National Chiao Tung University] at 06:29 21 November 2012

tri-iodide is considered to be first order in electron density [23]. According to the standard diffusion model for generation, transport and recombination of electrons, the rate of the electron density becomes expressed as [14,15,18,19,21,22]

$$\frac{\partial n}{\partial t} = G + D\frac{\partial^2 n}{\partial x^2} - \frac{n - n_0}{\tau} \tag{1}$$

in which n represents the temporally dependent electron density under illumination, n_0 the equilibrium electron density in the dark, G the rate of eletron generation, D the chemical diffusion coefficient of electrons and τ the electron lifetime. Because both D and τ depend on n controlled by the light intensity [14], the temporally resolved measurements should be conducted with a pulse excitation of small amplitude as a perturbation probe superimposed on a constant bias illumination. Supposing that the electron densities in the CB of TiO_2 induced by the bias and bias + probe light are n_1 and n_2, respectively, the electron density induced by the probe pulse ($\Delta n = n_2 - n_1$) is expected to be much less than n_1; G, D and τ are then regarded as constant parameters when Δn is probed as a function of time. This requirement is fundamental for all measurements of small amplitude introduced in this review. Under a condition $\Delta n \ll n_1$, the rate equation for Δn based on Equation (1) becomes simplified to

$$\frac{\partial \Delta n}{\partial t} = D\frac{\partial^2 \Delta n}{\partial x^2} - \frac{\Delta n}{\tau} \tag{2}$$

Equation (2) might be solved easily in separate steps under two extreme conditions as demonstrated in Figure 2. Under a short-circuit condition, only diffusion is considered; the last term in Equation (2) is neglected. This diffusion equation, known as Fick's second law, becomes solvable depending on appropriate boundary conditions. For the back-contact electrode (conducting glass) located at $x = 0$ and the electrons concentrated at $x = L$ at $t = 0$, the solution of Equation (2) is obtained as [24]

$$\Delta n_{\mathrm{SC}}(x, t) = \frac{\Delta N}{2\sqrt{\pi D\, t}} \exp\left[-\frac{(x - L)^2}{4Dt}\right] \tag{3}$$

in which L represents the thickness of the TiO_2 layer; ΔN represents the density of injected electrons (in unit cm^{-2}) induced by the probe pulse at time zero. For photocurrent decays, the electron densities $\Delta n_{\mathrm{SC}}(x, t)$, in unit cm^{-3}, collected at the back-contact electrode ($x = 0$) are converted into temporally dependent current densities (in unit of $\mathrm{A\ cm}^{-2}$) [24],

$$\Delta J_{\mathrm{SC}}(t) = \frac{eL\Delta N}{2\sqrt{\pi D} t^{3/2}} \exp\left(-\frac{L^2}{4Dt}\right) \tag{4}$$

in which e denotes the elementary charge. A non-linear regression fitting of the photocurrent transient to Equation (4) yields values of parameters ΔN and D. Alternatively, instead of solving Equation (2), an empirical approach is applied on fitting the photocurrent transients according to a single exponential decay with collection time coefficient τ_{C}, via this equation [16,18],

$$\Delta J_{\mathrm{SC}}(t) = \Delta J \exp\left(-t/\tau_{\mathrm{C}}\right) \tag{5}$$

Downloaded by [National Chiao Tung University] at 06:29 21 November 2012

in which ΔJ is the pre-exponential factor signifying the amplitude of the photocurrent change induced by the probe pulse at time zero. The average diffusion coefficient D is correlated with τ_C [18]:

$$D = \frac{(L/2)^2}{t_{1/2}} = \frac{(L/2)^2}{\tau_C \ln 2} = \frac{L^2}{2.77\,\tau_C} \tag{6}$$

in which $t_{1/2}$ is the time to extract half of the injected electrons ($\Delta N/2$) at the middle of the film ($L/2$). This approach is purely empirical, and the photocurrent transient might be fitted poorly with a single exponential decay function. When a multiple exponential decay function is applied, the electron collection time is obtained with an amplitude-weighted value ($\bar{\tau}_C = \sum_i A_i \tau_i / \sum_i A_i$; the amplitude A_i and the decay coefficient τ_i were obtained from a non-linear curve fitting of experimental data $S(t)$ with a multi-exponential decay function according to $S(t) = \sum_i A_i e^{-t/\tau_i}$); the diffusion coefficient is determined from $D = L^2/(2.77\ \bar{\tau}_C)$.

Under an open-circuit condition, only the recombination term is involved in Equation (2). The solution of Equation (2) becomes simply a single exponential decay function:

$$\Delta n_{OC}(t) = \Delta N \exp\left(-\frac{t}{\tau_R}\right) \tag{7}$$

in which τ_R represents the time coefficient for charge recombination. For photovoltage decays, the transients representing the recombination electron densities are well fitted with a single exponential decay function [16,18],

$$\Delta V_{OC}(t) = \Delta V \exp(-t/\tau_R) \tag{8}$$

in which ΔV is the pre-exponential factor giving the amplitude of the voltage change induced by the probe pulse at time zero.

Equation (8) is an effective approximation to obtain the electron lifetime at the open-circuit condition because the decay ΔV_{OC} is well correlated with the decay of the electron density formulated in Equation (7), according to the following details. As shown in Figure 3(a), electron densities n_1 and n_2 fill the CB of TiO_2 to Fermi levels V_{F1} and V_{F2}, respectively, which give open-circuit voltages V_1 ($=V_{F1} - V_{F0}$) and V_2 ($=V_{F2} - V_{F0}$) with respect to the Fermi level of the redox couple (V_{F0}). With the system at thermal equilibrium, n_1 and n_2 are related to V_1 and V_2 via $n_1 = n_0\, e^{qV_1/kT}$ and $n_2 = n_0\, e^{qV_2/kT}$, respectively. The difference of photovoltage ΔV ($=V_2 - V_1$) at time zero thus becomes related to ΔN ($=n_2(0) - n_1$) according to these formulae:

$$\Delta V = V_2 - V_1 = \frac{kT}{q}\ln\frac{n_2}{n_1} = \frac{kT}{q}\ln\left(\frac{\Delta N}{n_1} + 1\right) \cong \frac{kT}{q}\cdot\frac{\Delta N}{n_1} \tag{9}$$

To obtain the above result, criterion $\Delta N \ll n_1$ must be fulfilled. Because k, T, q and n_1 are constants, the perturbation of small amplitude of the probe ensures that ΔV is proportional to ΔN. The ΔV_{OC} decay (Figure 3c) is similarly related to the Δn_{OC} decay (Figure 3b) through combination of the results obtained from Equations (7) and (9),

$$\Delta V_{OC}(t) \cong \frac{kT}{q}\cdot\frac{\Delta n_{OC}(t)}{n_1} = \frac{kT}{q}\cdot\frac{\Delta N}{n_1}\exp\left(-\frac{t}{\tau_R}\right) = \Delta V \exp\left(-\frac{t}{\tau_R}\right) \tag{10}$$

for which the result of Equation (8) is obtained.

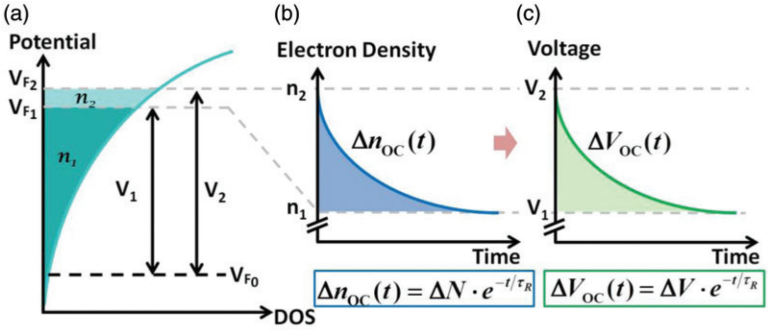

Figure 3. (Colour online) Schematic representations of (a) potential vs. density of trap states (DOS), (b) Δn_{OC} vs. time and (c) ΔV_{OC} vs. time at the open-circuit condition showing the relaxation for the potential difference ($\Delta V = V_2 - V_1$) and the population difference of electron densities ($\Delta n = n_2 - n_1$).

Downloaded by [National Chiao Tung University] at 06:29 21 November 2012

2.2. *Experiment*

Figure 4 depicts the experiment for a typical photoelectric measurement system [25]. The transient measurements are based on a large bias illumination generated with a CW diode laser to produce the photocurrent density (J_{SC}) and the photovoltage (V_{OC}) under short-circuit and the open-circuit conditions, respectively. To probe the transient decays, a pulsed YAG laser (pulse duration ~10 ns) is employed to perturb the photostationary state for which the transient profiles, either $\Delta J_{SC}(t)$ or $\Delta V_{OC}(t)$, are describable with a suitable kinetic model introduced in Section 2.1. Because the probe pulse is generated on a nanosecond scale, the detailed kinetic information for electron transport on TiO_2 films through a diffusion model is obtained from an analysis of the photocurrent transients according to Equation (4). As both electron transport and charge recombination in a typical DSSC device occur on a millisecond scale, an expensive pulsed laser as a probe can be replaced with a less costly LED source; only the decay parts of the transients are analyzed according to Equations (5)–(8).

Figure 5 shows the experimental design for the transient photoelectric (TCD and TVD) measurements using two LED lamps for bias and probe excitations labeled LED1 and LED2, respectively [26]. Typically bias LED1 is a white-light source and the wavelength of the probe LED2 may be selected at a particular value (blue, green or red colour) appropriate for the sensitisers used for the device. The intensities of the light sources are controlled with a multi-channel power supply triggered with a computer-controlled pulse generator (PG). The transients are recorded with an oscilloscope triggered with the PG. The conditions of short circuit and open circuit are controlled by a rapid electronic switch also triggered with the PG: the switch is off for the voltage transients recorded at the open-circuit condition (shown as blue lines) or on for the current transients recorded at the short-circuit condition (shown as red lines). A small resistance (e.g., 50 Ω) is introduced into the path of the short circuit to convert the currents into voltages to record the transients on an oscilloscope. The same system can operate for measurements of charge extraction (CE) to extract electron densities in the CB of TiO_2 under bias irradiations (only LED1 on) under the open-circuit condition.

Downloaded by [National Chiao Tung University] at 06:29 21 November 2012

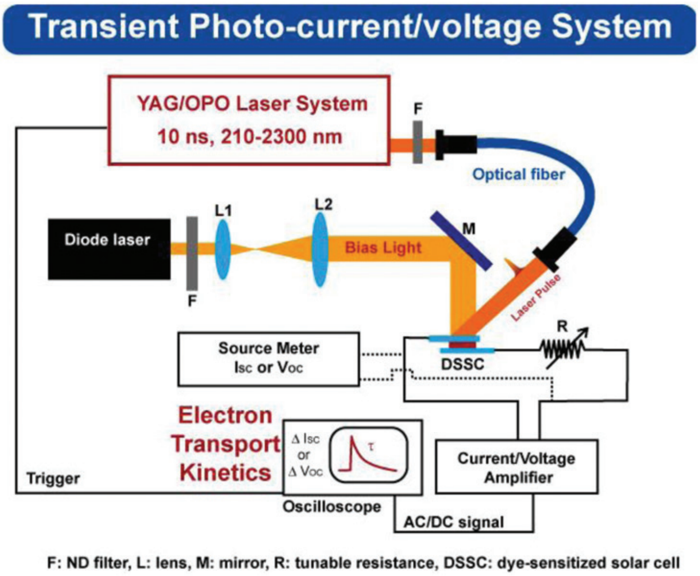

Figure 4. (Colour online) Experiment to measure photocurrent and photovoltage decays with the excitation probe with a pulsed laser [25].

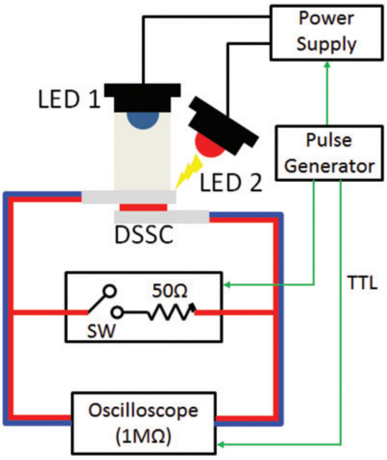

Figure 5. (Colour online) Experiment to measure photocurrent and photovoltage decays based on LED bias and probe lamps [26].

Figure 6(a) and (b) shows the timing charts for the CE and TCD/TVD measurements, respectively. For the CE method (Figure 6a), LED1 is fired under the open-circuit condition for duration Δt_1 and is then turned off at the same time that the system is switched to the short-circuit condition [27,28]. The current transient under the short-circuit

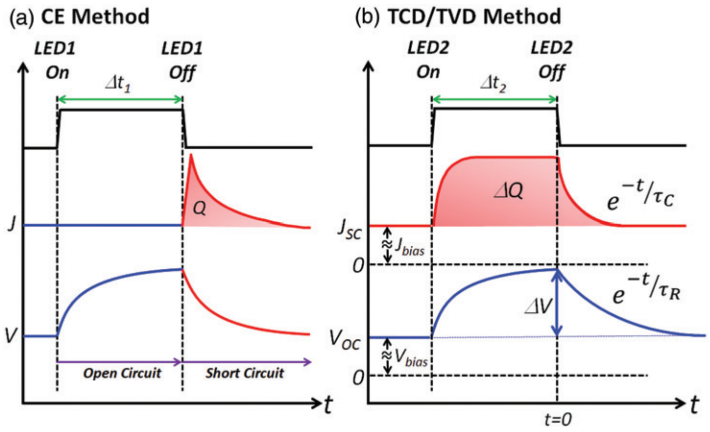

Figure 6. (Colour online) Timing charts for (a) CE and (b) TCD/TVD methods based on LED1 (bias light) and LED2 (probe excitation) under short-circuit (red traces) or open-circuit (blue traces) conditions [26].

condition is then recorded with an oscilloscope, from which the extracted charge density ($Q_{\mathrm{CE}}/\mathrm{C\,cm^{-2}}$) is obtained on integration of the current transient vs. time; the total charge density per volume ($N_e/\mathrm{cm^{-3}}$) upon bias LED1 illumination under the open-circuit condition is determined with [29]

$$N_e = \frac{Q_{\mathrm{CE}}}{e\,L\,(1-p)} \tag{11}$$

in which e is elementary charge, L is the thickness of the TiO_2 film and p is the porosity of TiO_2.

For the TCD/TVD methods (Figure 6b), LED1 serves as a bias lamp for the system to maintain bias irradiation in a steady state. The LED2 is fired superimposed on the LED1 illumination under either a short-circuit or an open-circuit condition for duration Δt_2; LED2 is turned off at the time defined as zero ($t = 0$). The resulting photocurrent transient (red curve) and the photovoltage transient (blue curve) are recorded on an oscilloscope to reflect the decays for the charge collection time coefficient (τ_{C}) and the charge recombination time coefficient (τ_{R}) under the short-circuit and the open-circuit conditions, respectively [15–18]. Although the kinetics obtained under the short-circuit condition involve both electron transport and charge recombination, the electron lifetimes are usually dominated process at short circuit to determine τ_{C}, the efficiency of charge collection (η_{CC}) can be thus obtained according to the following equation [17,30] under the criterion of high collection efficiency [31]:

$$\eta_{\mathrm{CC}} = \frac{\tau_{\mathrm{C}}^{-1} - \tau_{\mathrm{R}}^{-1}}{\tau_{\mathrm{C}}^{-1}} = 1 - \frac{\tau_{\mathrm{C}}}{\tau_{\mathrm{R}}} \tag{12}$$

Strictly speaking, τ_{C} and τ_{R} should be measured under the same Fermi level in order to determine η_{CC} appropriately [3]. There are many methods developed for this purpose, either by a direct [32,33] or an indirect approach [34,35].

Downloaded by [National Chiao Tung University] at 06:29 21 November 2012

Downloaded by [National Chiao Tung University] at 06:29 21 November 2012

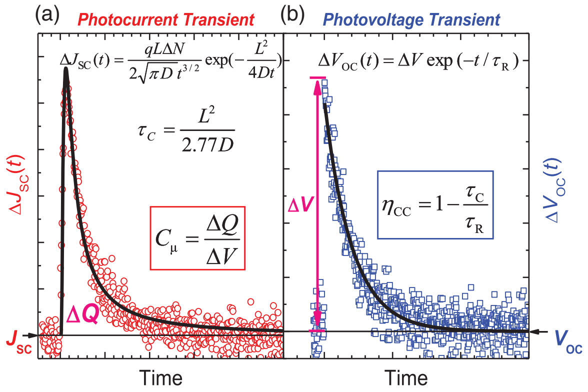

Figure 7. (Colour online) Typical photoelectric transients of (a) photocurrent decays and (b) photovoltage decays representing the kinetic processes electron transport and charge recombination of a DSSC under short-circuit and open-circuit conditions, respectively [25]. Reproduced by permission of the PCCP Owner Societies.

The charge density ΔQ due to the probe light irradiation is obtained through time integration of the current transient determined under the short-circuit condition; the potential difference ΔV due to the probe irradiation is the time-zero amplitude determined under the open-circuit condition (Figure 6b). The chemical capacitance (C_μ) measured at the Fermi level of CB of TiO_2 is obtained with [29]

$$C_\mu=\frac{\Delta Q}{\Delta V} \tag{13}$$

in which C_μ is proportional to the density of trap states (DOS) at the V_{OC} level under the bias irradiation. Specifically, C_μ is measured with the probe perturbation under bias irradiation to reflect the DOS at that Fermi level giving the V_{OC}. The information obtained from the plots of C_μ vs. V_{OC} for various materials (e.g., dyes, semiconductors, or electrolytes) provides direct evidence for the positions of the TiO_2 conduction band edge potentials corresponding to the devices under investigation.

2.3. *Data analysis*

Figure 7(a) and (b) shows typical photocurrent and photovoltage transients generated with a laser pulse under the bias irradiation; the equations and key parameters to characterise these transient decays according to Equations (4)–(8) are indicated therein. For the photocurrent $\Delta J_{SC}(t)$ decay (Figure 7a), a non-linear fitting of the photocurrent transient to Equation (5) evaluates parameters ΔN and D, and the charge collection time τ_C is obtained according to Equation (6) for known film thickness L; the charge density ΔQ due to the probe excitation is obtained on time integration of the current transient. For the photovoltage $\Delta V_{OC}(t)$ decay (Figure 7b), a linear fit of the logarithmic transient according to Equation (8) yields parameters ΔV and electron lifetime τ_R. The charge-collection efficiency (η_{CC}) and the chemical capacitance (C_μ) of the system thus become determined according to Equations (12) and (13), respectively.

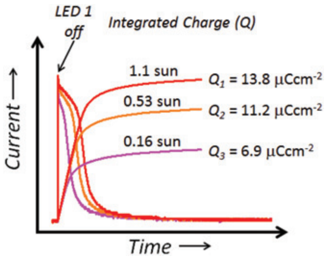

Figure 8. (Colour online) Three typical current transients obtained with the CE method under bias intensities as indicated. Extracted charge densities Q_1, Q_2 and Q_3 are obtained through integration of the corresponding transients with time [26].

Downloaded by [National Chiao Tung University] at 06:29 21 November 2012

Instead of a pulsed laser for probe excitation, in the following we demonstrate typical transient data obtained with a LED source as the bias and probe illumination (Figures 5 and 6) and provide the details of their data analysis. Figure 8 shows the short-circuit transients obtained from CE measurements with three bias CW (LED1) intensities corresponding to 0.16, 0.53 and 1.1 sun irradiations (1 sun irradiation is equal to 100 mW cm^{-2}). The irradiation period of LED1 (Δt_1) is set to ~200 ms at the open-circuit condition to ensure that the photovoltage attained a photostationary level; then LED1 is terminated while the device is simultaneously switched to a short-circuit condition. The resulting current transients attained after the switch is turned into the short-circuit condition are then integrated with time to obtain extracted charge densities Q_1, Q_2 and Q_3 indicated in the plots. The corresponding charge densities (N_e) under the three bias light irradiations are obtained according to Equation (11).

For the TCD and TVD measurements under the same three bias LED1 irradiations, the probe lamp (LED2) is fired with irradiation duration $\Delta t_2 \sim 50$ ms. The probe beams thus generate carriers causing a slightly increased photocurrent (ΔJ_{SC}) near J_{SC} of the cell under the short-circuit condition (Figure 9a), or a slightly increased photovoltage (ΔV_{OC}) near V_{OC} of the cell under the open-circuit condition (Figure 9b), subject to the intensities of the bias irradiations; the current and voltage decays are thereby measured according to typical traces in Figure 9(a) and (b), respectively.

To ensure that the small-amplitude perturbation criterion ($\Delta N \ll n_1$) of the system is fulfilled, the intensity of the probe is adjusted to be less than ~5% of the bias intensity. In a practical case, we control the intensities of the LED2 to maintain the device at a constant ΔV (typically less than 5 mV) much less than their V_{OC}. In this particular case (Figure 9) the LED2 is controlled to give $\Delta V_1 = \Delta V_2 = \Delta V_3 \sim 3.95$ mV under the open-circuit condition; those intensities yield probe-induced charge densities $\Delta Q_1 = 70$, $\Delta Q_2 = 35$ and $\Delta Q_3 = 14$ μC cm^{-2}, under the short-circuit condition; the three bias intensities were fixed at 110, 53 and 16 mW cm^{-2}, respectively. Figure 9(a) and (b) shows the corresponding decays of $\Delta J_{SC}(t)$ and $\Delta V_{OC}(t)$, respectively, from which relaxation time coefficients τ_C and τ_R are obtained on fitting the data according to Equations (5) and (8), respectively. Similarly, the charge-collection efficiency (η_{CC}) and the chemical capacitance (C_μ) of the system under the three bias irradiations are determined according to Equations (12) and (13), respectively.

Downloaded by [National Chiao Tung University] at 06:29 21 November 2012

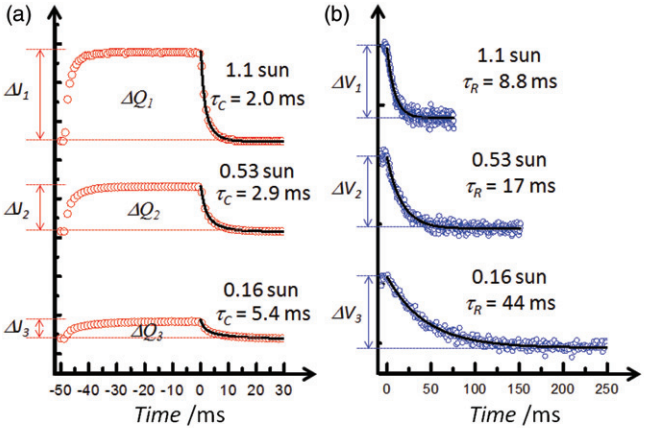

Figure 9. (Colour online) Typical photoelectric transients of (a) photocurrent decays and (b) photovoltage decays with LED2 as a probe lamp showing data obtained under three specific bias intensities generated by LED1 (1 sun = 100 mW cm^{-2}). For (a), $\Delta Q_1 = 70$, $\Delta Q_2 = 35$ and $\Delta Q_3 = 14\,\mu C\,cm^{-2}$; for (b) $\Delta V_1 = \Delta V_2 = \Delta V_3 \sim 3.95\,mV$ [26].

2.4. *Examples of temporally resolved techniques*

The temporally resolved techniques introduced in the preceding section have been widely applied to understand the kinetics of electron transport and charge recombination affecting the device performance of a DSSC system with various key components such as Ru complexes [6,7,27,36–45], organic dyes [11,12,46–62], porphyrins [9,25,63,64], TiO_2 [65–68], electrolytes [18,69–76] and in the solid-state devices. Photosensitisers such as Ru and porphyrin dyes are of particular interest because they play key roles in promoting the device performance with great hopes for future commercialisation. In the following, we describe how transient photoelectric measurements are applied to understand the transport and recombination of the devices in relation to the corresponding photovoltaic performance of three specific systems – (a) push-pull porphyrins [64], (b) heteroleptic Ru dyes [77], and (c) nanooctahedral TiO_2 [78,79].

(a) Porphyrins

Porphyrins are promising candidates as highly efficient sensitisers for DSSC because of their superior light-harvesting ability in the visible region [80–90]. Recent advances in the development of a push–pull zinc porphyrin sensitiser (YD2-oC8) with co-sensitisation of an organic dye using a cobalt-based electrolyte attained efficiency 12.3% of power conversion [9], which is superior to devices developed based on Ru complexes [6–8] and becomes a new benchmark in this area. The key structural feature for molecular design of a highly efficient porphyrin sensitiser is to have long alkoxyl chains in the *ortho*-positions of the *meso*-phenyls so as to envelope effectively the porphyrin ring to decrease the degree of dye aggregation for an increased electron injection yield and to form a blocking layer to increase the charge collection yield [91]. In the following, we provide an example to show how the TCD and TVD techniques can help us to understand the structural feature of such a molecular design affecting the photovoltaic performances of the devices made of two porphyrin sensitisers, LD13 and LD14 (Figure 10) [64].

Downloaded by [National Chiao Tung University] at 06:29 21 November 2012

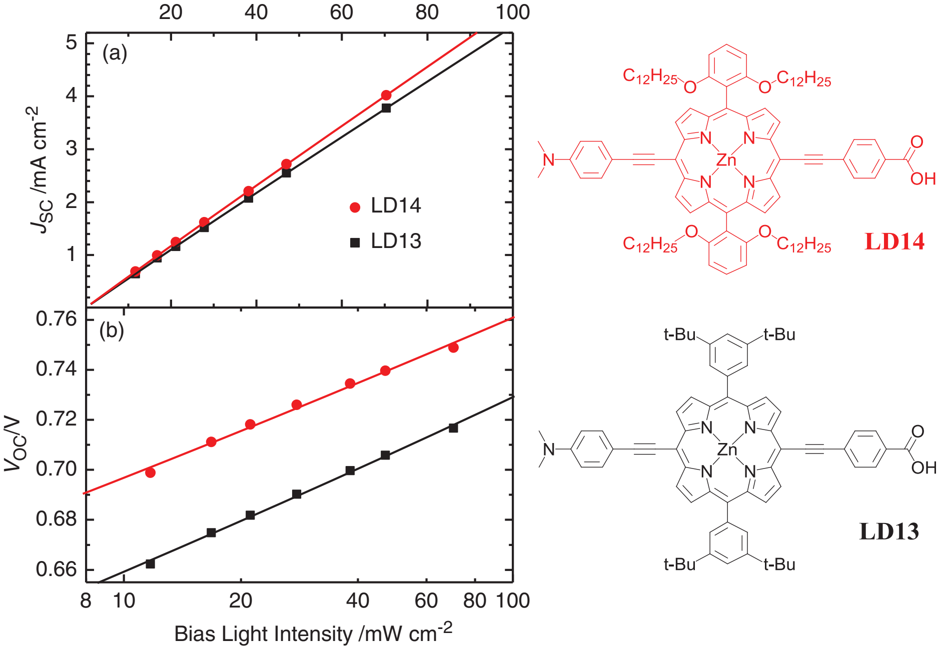

Figure 10. (Colour online) (a) Short-circuit photocurrent density (J_{SC}) and (b) open-circuit photovoltage (V_{OC}) of devices made of two porphyrin dyes (LD13 and LD14, the corresponding molecular structures are indicated in the right-hand side) as a function of bias intensity on a linear scale (a) or on a logarithmic scale (b) [64].

Both LD13 and LD14 devices exhibit excellent performances (9.3 vs. 10.2%), but the latter shows a V_{OC} value (736 mV) greater than that (697 mV) of the former that accounts mostly for the discrepancy of the performances. The transient photoelectric measurements are performed with a thin TiO_2 film (thickness $L = 1.5\,\mu m$) for the two devices under seven bias light irradiations with the intensities in a range 12–70 mW cm^{-2}. Figure 10(a) and (b) shows linear plots of J_{SC} vs. the bias intensities (I_0) and semi-logarithmic plots of V_{OC} vs. I_0, respectively. The results indicate that the photocurrents of LD14 are slightly larger than those of LD13, but the photovoltages of LD14 are significantly larger than those of LD13, consistent with the performances of the corresponding optimised devices [64].

Figure 11(a) and (b) shows logarithmic plots of τ_C vs. I_0 and τ_R vs. I_0 for the results obtained from the TCD and TVD measurements, respectively. The results display a systematic trend for the discrepancies between τ_C and τ_R.

Figure 12 shows plots of C_μ vs. V_{OC} for the LD13 and LD14 devices. As C_μ is proportional to the DOS of TiO_2 at each V_{OC}, the plots shown in Figure 12 provide direct information about the shift of the conduction band edge of TiO_2 upon dye uptake. The results indicate that there exists an apparent potential shift upward by 24 mV for LD14 relative to LD13, which is consistent with the enhancement of V_{OC} of the corresponding devices upon optimisation.

Downloaded by [National Chiao Tung University] at 06:29 21 November 2012

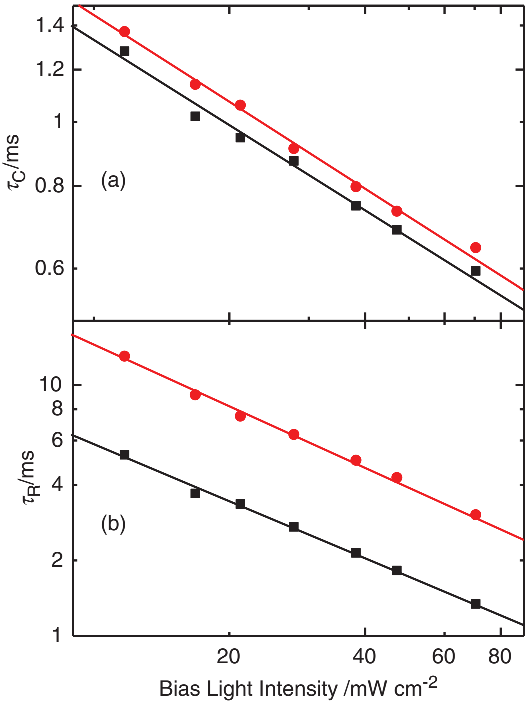

Figure 11. (Colour online) Logarithmic plots of (a) electron collection time τ_C and (b) electron lifetime τ_R as a function of bias intensity for devices made of LD13 and LD14 [64]. τ_C and τ_R were determined from TCD and TVD measurements, respectively.

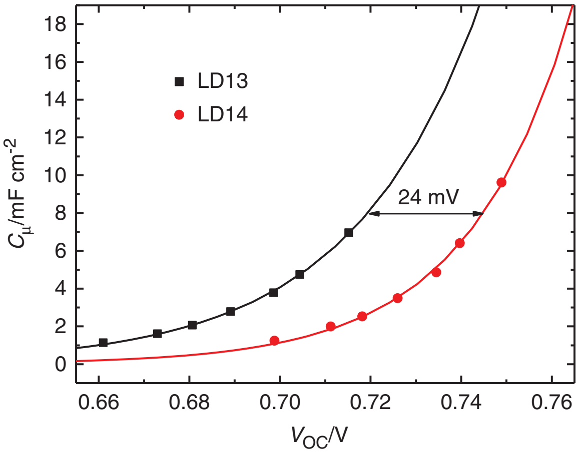

Figure 12. (Colour online) Chemical capacitance ($C_\mu = \Delta Q/\Delta V$) vs. V_{OC} for devices made of two porphyrin dyes (LD14 and LD13) showing a potential shift 24 mV as indicated [64].

Downloaded by [National Chiao Tung University] at 06:29 21 November 2012

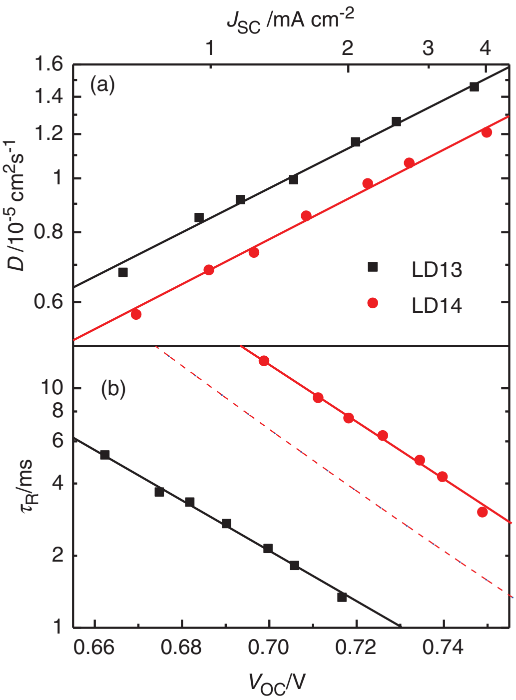

Figure 13. (Colour online) (a) Logarithmic plots of diffusion coefficient (D) vs. J_{SC} and (b) semi-logarithmic plots of recombination time (τ_R) vs. V_{OC} for devices made of LD13 and LD14 under bias irradiation at seven intensities [64]. D was determined according to Equation (6) with TiO_2 film thickness $L = 1.5\,\mu m$. The dashed line in (b) shows the data of the LD14 device with a potential displacement according to the shifts indicated in Figure 12.

Figure 13(a) and (b) shows logarithmic plots of D vs. J_{SC} and semi-logarithmic plots of τ_R vs. V_{OC}, respectively, to compare the kinetics of electron transport and charge recombination for devices LD13 and LD14. The diffusion coefficients of LD13 are greater than those of LD14 because the smaller TiO_2 conduction band edge potential of the former might lead to a deeper electron injection [13] and more rapid electron transport than of the latter.

Owing to the shift upward of the TiO_2 conduction band edge potential for LD14 with respect to LD13, a fair comparison of the degree of charge recombination should be made at the same reference potential level. As a result, the potential scale of τ_R is decreased by 24 mV for LD14 so that the electron lifetimes become compared at the same 'equivalent common conduction band' level [20]. The shifted plot τ_R vs V_{OC} of the LD14 device is indicated as a dashed line in Figure 13(b). After correction for the shift of the conduction band edge of TiO_2 for LD14, we still observe τ_R for LD14 to be significantly greater than for its reference LD13. This result indicates that the *ortho*-substituted long alkoxy chains play a key role to prevent approach of I_3^- in the electrolyte to the surface of TiO_2 so as to retard the electron interception at the electrolyte/TiO_2 interface. We conclude that, in addition to the increased conduction band edge of the TiO_2 potential, the retarded charge

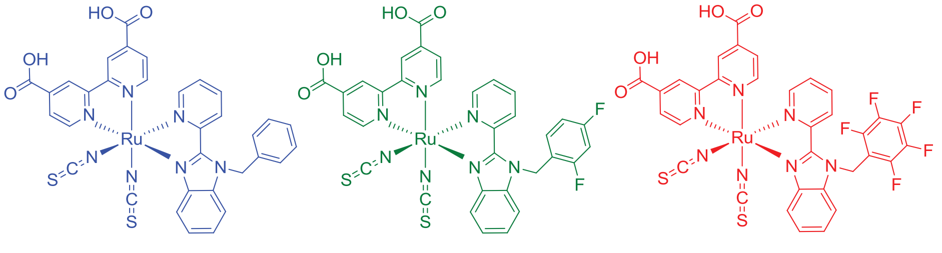

Figure 14. (Colour online) Molecular structures of three ruthenium dyes, RD5, RD12 and RD15 [97].

Downloaded by [National Chiao Tung University] at 06:29 21 November 2012

recombination is a factor to account for the enhanced V_{OC} of device LD14 relative to device LD13.

The strategy to improve V_{OC} for organic dyes has attracted many profound investigations [3–14]. Based on the results obtained from transient photoelectric measurements, the shift of the TiO_2 conduction band for devices made of organic dyes [12,48,92] and porphyrin dyes [93] was found to be small, supporting that the smaller V_{OC} of organic sensitizers relative to those of Ru complexes is due to their smaller electron lifetimes. Varied V_{OC} hence reflect varied electron lifetimes rather than varied positions of the conduction band [12]. Data for C_μ vs. V_{OC} of other organic systems reveal, however, potential shifts consistent with the trend of V_{OC} of the devices [30,94], similar to the results of the LD13/LD14 system introduced here.

(b) Ru dyes

The DSSC devices made of homoleptic ruthenium complexes (e.g., N3 and N719) attained an impressive efficiency, $\eta \sim 11\%$, of power conversion under one-sun illumination [1–3], but the enduring stability of the devices made of these complexes has become a major challenge. As a result, an amphiphilic Ru sensitizer (e.g., Z907) was developed to improve their durability [95,96]. One strategy to enhance the light-harvesting efficiency of the dye and to improve the long-term stability of the corresponding device is to replace one 4,4′-dicarboxylic-2,2′- bipyridine (dcbpy) anchoring ligand in the N3 dye with an ancillary ligand with electron-rich π-conjugated segments and long alkyl chains, forming a family of heteroleptic ruthenium complexes [6–8]. The example given here is based on heteroleptic ruthenium complexes in a series containing benzimidazole ligands (Figure 14), for which the device performance of reference dye RD5 was comparable to that of a N719 dye, but V_{OC} of RD5 was substantially less than that of N719 because of rapid recombination rate of charge in the former case [42]. Figure 14 shows the molecular structures of heteroleptic ruthenium dyes in a series with benzimidazole ligands containing fluorine atoms numbering none (RD5), two (RD12) and five (RD15). The devices made of RD5, RD12 and RD15 show a systematic variation with the number of fluorine atoms on the benzyl ring: V_{OC} increases with increasing number of fluorine atoms, but the corresponding J_{SC} values show the opposite trend. Transient photoelectric measurements would provide guiding kinetic information to rationalise their device performances.

Downloaded by [National Chiao Tung University] at 06:29 21 November 2012

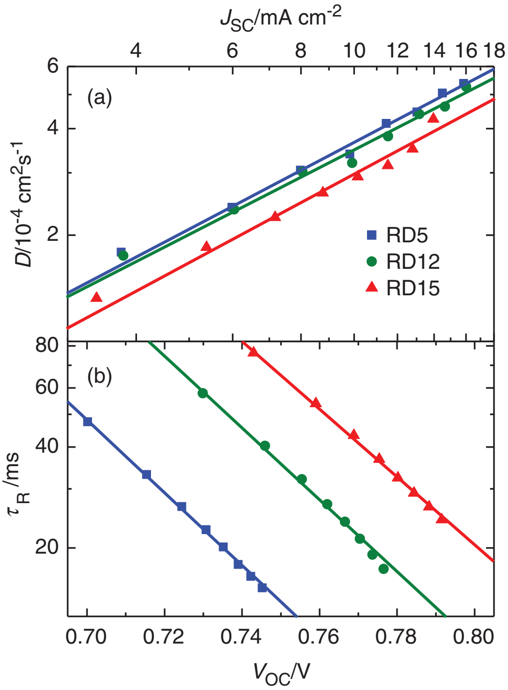

Figure 15. (Colour online) Electron-transport kinetics: (a) logarithmic plots of diffusion coefficient (D) vs. J_{SC} obtained from TCD measurements, and (b) semi-logarithmic plots of charge recombination coefficient (τ_R) vs. V_{OC} obtained from TVD measurements, for DSSC devices made of RD5, RD12 and RD15 under eight white bias light irradiations with a probe pulse (duration ~50 ms) at 630 nm [77].

Figure 15(a) and (b) shows logarithmic plots of D vs. J_{SC} and semi-logarithmic plots of τ_R vs. V_{OC}, respectively, to compare the electron transport and charge recombination kinetics for the devices made of LD5, RD12 and RD15 under eight bias irradiations. Regarding the results shown in Figure 15(a), D of RD5 is similar to that of RD12 but is significantly greater than that of RD15, indicating that transport of injected electrons is more rapid in the RD5 and RD12 devices than in the RD15 device. The results shown in Figure 15(b) exhibit similar slopes of the semi-logarithmic plots of the three systems but with order RD15 > RD12 > RD5, indicating that increasing the substitution of fluorine atoms on the phenyl group slows the charge recombination rate when a comparison is made at the same V_{OC}. The values of V_{OC} are determined by the location of the Fermi level within the band gap of TiO_2, which might be affected by the position of the potential or the charge recombination at the dye/TiO_2 interface. To make a fair comparison of charge recombination of the systems under investigation, we examined the shift of the conduction band of TiO_2 upon dye uptake. For this purpose, the charge densities at each V_{OC} were extracted via rapid switching to the short-circuit condition for the three systems.

The method of charge extraction determines the total extracted charges Q_{CE}/C cm^{-2} under bias irradiation that yields V_{OC}. We observed that the plots of N_e vs. V_{OC}, shown in

Downloaded by [National Chiao Tung University] at 06:29 21 November 2012

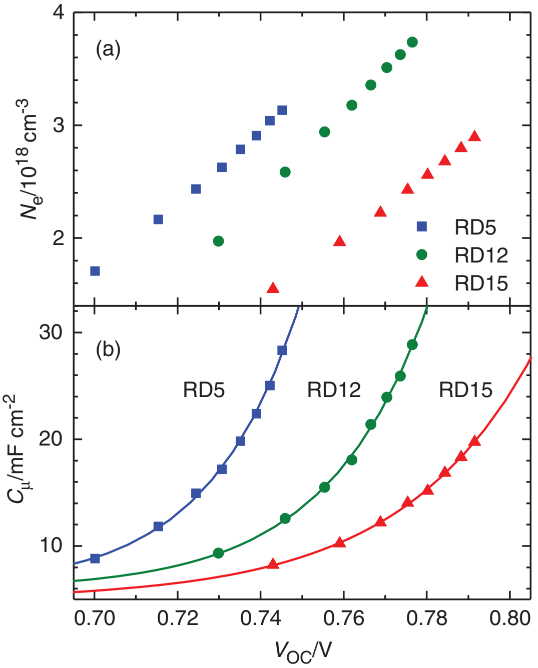

Figure 16. (a) Charge densities N_e obtained with the charge-extraction (CE) method and (b) chemical capacitances C_μ obtained from the transient photoelectric (TCD/TVD) measurements as a function of V_{OC} for DSSC devices made of RD5, RD12 and RD15 under eight white bias light irradiations [77].

Figures 16(a), exhibit variations similar to those in the plots of chemical capacitance ($C_\mu = \Delta Q/\Delta V$) vs. V_{OC} shown in Figure 16(b). We demonstrate here that both charge density N_e (obtained from the CE method) and chemical capacitance C_μ (obtained from the small-amplitude method) measurements give consistent results to confirm that, upon dye uptake, the TiO_2 conduction band edge potentials were shifted upward with order RD15 > RD12 > RD5, indicating that increasing substitution with fluorine atoms on the phenyl group shifts the potential of the conduction band edge of TiO_2 towards a more negative (upward) direction.

Figure 17 displays plots of τ_R vs. N_e for a comparison of the kinetics of charge recombination of the three devices at the same N_e level. The trend of the electron lifetimes was remarkably altered to RD12 > RD15 > RD5; the charge recombination between the CB electrons on the TiO_2 surface and the I_3^- species in the electrolyte became more significant for RD15 than for RD12 when both systems were compared at the same N_e level. In contrast, when both systems were compared at the same Fermi level (Figure 15b), larger τ_R were observed for RD15 than for RD12 because the injected electrons in RD15 were fewer than those in RD12 due to the upward shift of the TiO_2 conduction band edge potential upon dye uptake for the former (Figure 16). We draw three conclusions: (1) substitution with fluorine atoms in the benzimizadole ligand produces retarded charge

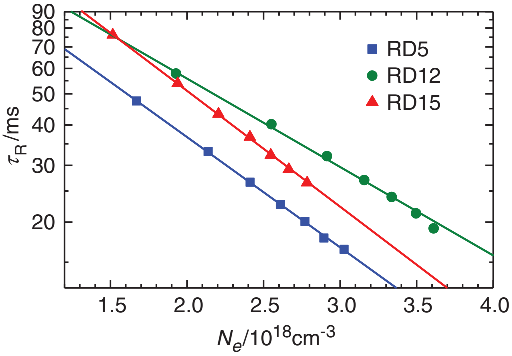

Figure 17. (Colour online) Charge recombination coefficient (τ_R) vs. charge density (N_e) obtained from transient photoelectric and charge-extraction measurements for DSSC devices made of **RD5**, **RD12** and **RD15** under eight irradiations with white bias light [77].

Downloaded by [National Chiao Tung University] at 06:29 21 November 2012

recombination due to the partial negative charge on the fluoro-substituted ligands; (2) increasing substitution of fluorine atoms shifts upward the band edge potential of TiO_2 but also increases the charge recombination rate; (3) as a compromise, the device made of RD12 has a smaller charge recombination rate than that of RD15 when they are compared at the same N_e (or DOS) level. The increase of V_{OC} upon fluoro-substitution is thus determined by two factors – an upward shift of the potential and a retardation of the charge recombination.

(c) Titania

To apply the CE and TCD/TVD methods for specific DSSC systems and to compare the results with those obtained from the IMPS/IMVS methods introduced in the next section, in the following we present as an example how these techniques were combined to acquire information to understand the kinetics of transport and recombination of the DSSC devices fabricated based on two TiO_2 films, labelled NP and HD; the corresponding SEM images showing the nanostructural morphologies are displayed in the right side of Figure 18. The details of the synthesis and characterisation of the nanostructural films are presented elsewhere [78].

Both NP and HD films were fabricated into DSSC devices using the N719 dye and showed promising photovoltaic performances. For the NP devices fabricated according to a conventional approach [98], the spherical nanoparticular morphology limits the total film thickness (L) to a large value, and the best performance (J_{SC}/mA cm^{-2} = 15.9, V_{OC}/mV = 808, FF = 0.747 and η = 9.6%) occurred at L = 18–20 μm. For the newly designed HD films with nano-octahedral morphology [78], devices with thicker films were fabricated to give the best performance (J_{SC}/mA cm^{-2} = 15.9, V_{OC}/mV = 825, FF = 0.776 and η = 10.2%) that occurred at L = 28 μm. To make a systematic comparison for these two films, we performed transient photoelectric measurements of these two devices at a similar film thickness ($L \sim 20$ μm) based on fourteen bias irradiations.

Under one-sun illumination (I_0 = 100 mW cm^{-2}), the photovoltaic performances of the two devices show the following results: for HD, J_{SC}/mA cm^{-2} = 17.54, V_{OC}/mV = 749,

Downloaded by [National Chiao Tung University] at 06:29 21 November 2012

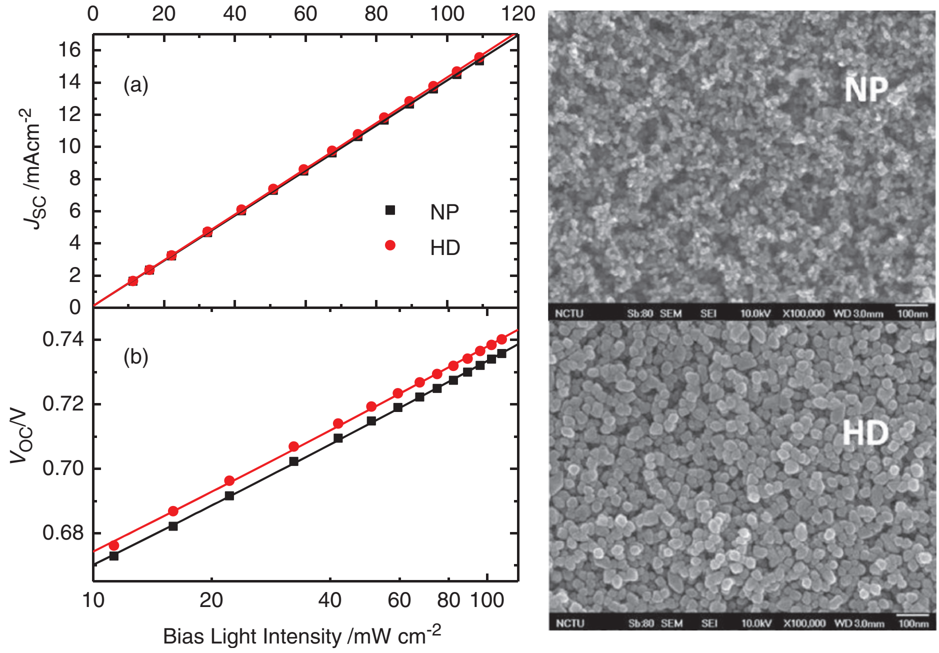

Figure 18. (Colour online) (a) Short-circuit current density (J_{SC}) and (b) open-circuit voltage (V_{OC}) of devices fabricated based on two TiO_2 films (NP and HD, the corresponding SEM images are shown in the right side [78]) as a function of bias intensity (I_0) on a linear scale (a) or on a logarithmic scale (b). The photosensitiser is N719 dye.

FF = 0.659 and $\eta = 8.66\%$; for NP, J_{SC}/mA cm^{-2} = 17.10, V_{OC}/mV = 745, FF = 0.649 and $\eta = 8.27\%$. The devices were then put into the temporally resolved system for the CE and TCD/TVD measurements. Figure 18(a) and (b) shows linear plots of J_{SC} vs. I_0 and semi-logarithmic plots of V_{OC} vs. I_0, respectively. These results indicate that, under the same bias light irradiation, the two devices have nearly the same photocurrent outputs, but the photovoltages of the HD device are greater than those of the NP device, consistent with the overall performances of the optimised devices.

Figure 19(a) and (b) shows the electron collection times (τ_C) and the electron lifetimes (τ_R) obtained from the TCD and TVD measurements, respectively, under the 14 bias light irradiations. The results show, remarkably, that, under bias light irradiation with the same intensity, the rates of electron transport of the HD device are much greater than those of the NP devices whereas the rates of charge recombination are exactly the same for both devices. These results feature the superior electron transport for HD films with respect to NP films.

Figure 20 shows plots of C_μ vs. V_{OC} for these two devices, indicating that the TiO_2 conduction band edge potential of the HD film was shifted slightly upward by ~4 mV compared to that of the NP film. Figure 21(a) and (b) shows plots of D vs. J_{SC} and τ_R vs. V_{OC}, respectively. The diffusion coefficients of the HD device are much greater than those of the NP device, as we have seen in Figure 19(a). In contrast, the almost identical electron

Downloaded by [National Chiao Tung University] at 06:29 21 November 2012

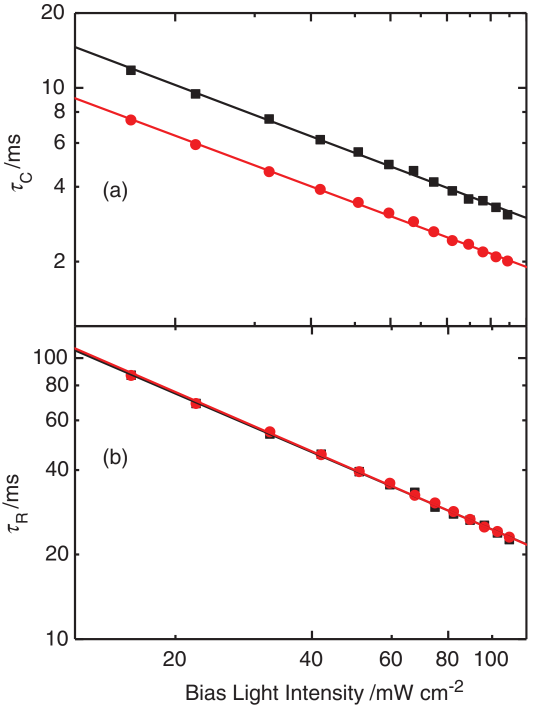

Figure 19. (Colour online) Logarithmic plots of (a) electron collection time (τ_C) and (b) electron lifetime (τ_R) as a function of bias intensity (I_0) of white light for devices made of NP and HD TiO_2 films [79]. τ_C and τ_R were determined from the TCD and TVD measurements, respectively.

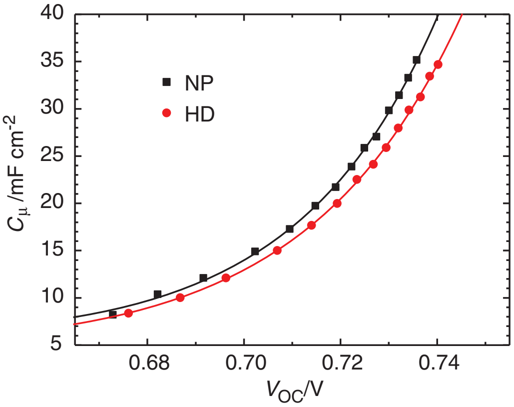

Figure 20. (Colour online) Plots of chemical capacitance ($C_\mu = \Delta Q/\Delta V$) vs. V_{OC} for the devices made of two TiO_2 films (NP and HD) showing an upward potential shift only ~4 mV for the HD film with respect to the NP film [79].

Downloaded by [National Chiao Tung University] at 06:29 21 November 2012

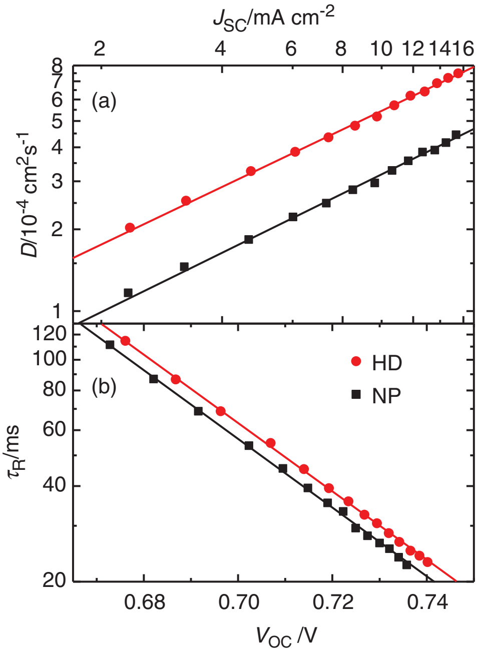

Figure 21. (Colour online) (a) Logarithmic plots of diffusion coefficient (D) vs. J_{SC} and (b) semi-logarithmic plots of recombination time (τ_R) vs. V_{OC} for devices fabricated with HD and NP under bias irradiation at fourteen intensities obtained from TCD and TVD measurements, respectively [79]. D is determined according to Equation (6) with TiO_2 film thickness $L = 20\,\mu m$.

lifetimes of the two devices compared at the same bias intensities (Figure 19b) show a slightly different feature (HD > NP for τ_R) when both are compared at the same V_{OC} level (Figure 21b). On taking into account the slightly upward shift of the TiO_2 conduction band edge potential of the HD film with respect to the NP film, the rates of charge recombination are expected to be similar for both devices.

The CE measurements were performed under the same fourteen bias light irradiations. Figure 22(a) shows plots of V_{OC} vs. N_e for the two devices, indicating that the TiO_2 conduction band edge potential of the HD film locates above that of the NP film, consistent with the results of C_μ vs. V_{OC} shown in Figure 20, but the scale of the potential shift between the two films shown in Figure 22(a) is larger than that shown in Figure 20: for the former the potential shift was ~10 mV at small intensity and increased to ~20 mV at large intensity based on the CE measurements; for the latter the shift was only ~4 mV at all intensities based on the small-amplitude measurements. Because of the larger displacement of the TiO_2 potential evaluated with the CE method, the charge recombination times (τ_R) of the HD device become slightly smaller than those of the NP devices (Figure 22b) when they are compared at the same N_e level determined by the CE method.

To compare the photovoltaic performances of the two devices, the larger V_{OC} of the HD device might be due to a small upward shift of the TiO_2 conduction band edge potential, but the electron diffusion is much more rapid for HD than for NP that led to

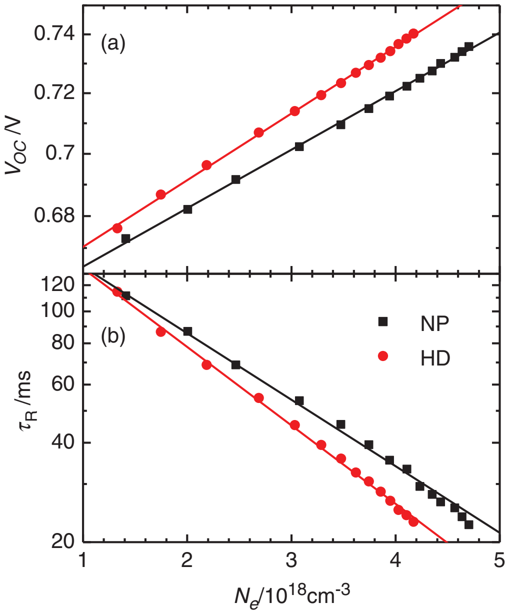

Figure 22. (Colour online) (a) Open-circuit voltage (V_{OC}) and (b) electron lifetimes (τ_R) as a function of charge density (N_e) for devices fabricated with HD and NP films under fourteen bias light irradiations [79]. The results were obtained from the CE and TVD measurements.

much greater charge-collection efficiency for the HD film than for the NP film. The effect of particle size of the NP films was investigated based on the TCD measurements for nanoparticles with size over a broad range [68,99]. The results indicate that the diffusion coefficients increase with increasing particle size, but the rates of charge recombination also increase with increasing particle size [68,99]. The HD film has the advantage of more rapid electron transport because of its larger size than the conventional NP film, but does not lose its advantage in maintaining electron lifetimes similar to those of the NP film with smaller particle size. The electron transport property of the HD film is superior such that the devices with much thicker films are fabricated to improve the device performance relative to devices made of NP films.

Another system investigated with the CE and TCD/TVD methods is that of Nb-doped TiO_2 reported by Grätzel and co-workers [66]. In that investigation, the devices made of Nb-doped films exhibited a systematic variation of photovoltaic performance: J_{SC} increased while V_{OC} decreased upon increasing Nb doping levels from 0.5% to 2%. The performance of the best device attained $\eta = 8.1\%$ at the 0.5% level. These CE results indicate that Nb-doping entails a downward shift of the conduction band edge, and the greater doping concentrations cause more downward potential shifts. The TVD measurements indicate that Nb-doping has the effect of retarding charge recombination in a systematic trend, but the TCD results reveal that electron transport slows on Nb-doping; both effects compensate such that a device at the 0.5% doping level shows the best performance.

Downloaded by [National Chiao Tung University] at 06:29 21 November 2012

Downloaded by [National Chiao Tung University] at 06:29 21 November 2012

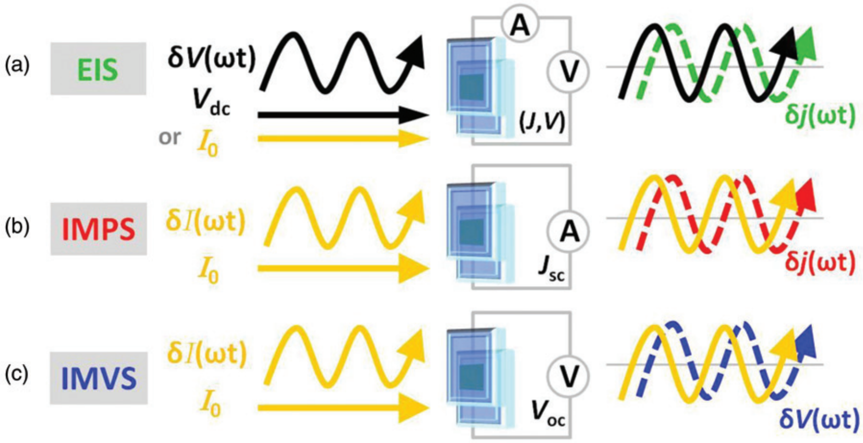

Figure 23. (Colour online) Representations of operating principles for frequency-domain measurements of (a) EIS, (b) IMPS and (c) IMVS. The solid waves represent a small ac potential (for EIS) or sinusoidally intensity-modulated light (for IMPS and IMVS) as perturbations to obtain the frequency responses under the bias dc potentials (for EIS) or the bias cw illumination (for all techniques). The electric responses (shown as dashed waves) have the same frequency as the perturbation but vary in amplitude and phase angle.

3. Measurements of impedance spectroscopy

3.1. *Principle*

Impedance Spectroscopy (IS) is an electrochemical technique (also named EIS) based on an analysis of frequency response, and has broad applications [100]. Any intrinsic interfacial property of materials, nanostructures and composition, or external factors, such as temperature, bias potential, illumination and pressure that influences the charge flow throughout the device causing a time lag and a measurable phase angle, can be well characterised with EIS. For our purpose, this technique is capable of analyzing the kinetics of complicated interfacial processes in a DSSC device highlighted in Figures 1 and 2; the key factors governing the photovoltaic performance of the device are well understood [14,19,20,101] because they provide information about charge transfer across interfaces, accumulation of charge at interfaces and charge transport in materials [102–105].

The general approach of EIS is to apply a sinusoidal potential perturbation to the electrodes or devices and to observe the current response, or vice versa. As shown in Figure 23(a), an ac voltage modulation of small amplitude (δV) is superimposed on a desired dc bias potential (V_{dc}) or a constant cw bias irradiation (intensity I_0); a current response (δj) is measured for frequency ($f = \omega/2\pi$) over a sufficiently wide range. If the ac potential of small amplitude is replaced with a sinusoidally modulated lamp with small intensity (δI, expressed as photon flux) superimposed on a constant cw bias irradiation (I_0), this IS technique is related to intensity-modulated photocurrent spectroscopy (IMPS) or intensity-modulated photovoltage spectroscopy (IMVS). For IMPS [31], the magnitude and phase shift of the current response (δj) with respect to the modulation of incident intensity (δI) are measured as a function of f (Figure 23b); for IMVS [106]; those of the voltage response (δV) with respect to δI are measured as a function of f (Figure 23c).

Downloaded by [National Chiao Tung University] at 06:29 21 November 2012

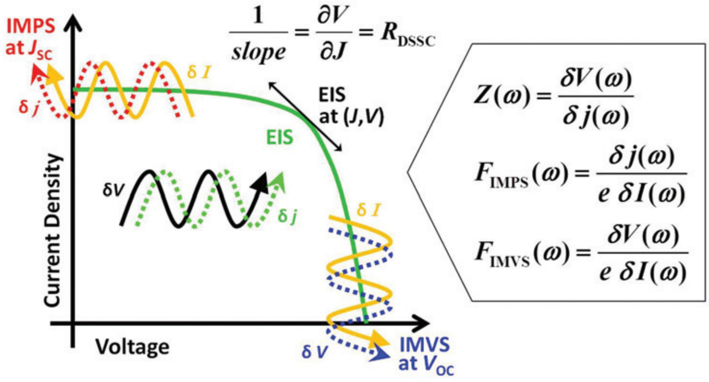

Figure 24. (Colour online) Schematic representations of impedance analysis with a relation between current-voltage curves and impedance responses. The EIS measurements are performed at a selected steady-state point along the *J–V* curve whereas IMVS and IMPS measurements are made solely under open-circuit and short-circuit conditions, respectively.

One relates the current–voltage (*J–V*) curve of a DSSC to the EIS results on measuring EIS at a specific (*J*, *V*) point under conditions of the same bias intensity I_0 [107–109]. As shown in Figure 24, impedance $Z(\omega) = \delta V(\omega)/\delta j(\omega)$ at the low- frequency limit ($\omega \to 0$) corresponds to the reciprocal of the slope at the steady state of the *J–V* curve, which is the resistance of the device (R_{DSSC}). Analysis of the EIS response enables not only reconstructing the *J–V* characteristic of the device but also distinguishing the circuit elements related to the physicochemical processes in a device [108–110]. Interested readers might refer to the reviews published by Halme and co-workers [19] and by Bisquert and co-workers [20] on the theory of EIS and its applications on DSSC.

Different from EIS measurements, the intensity-modulated methods, IMPS and IMVS, are based on modulated light intensity of small amplitude (δI). For the IMPS method, the current response (δj) is measured and the frequency-dependent IMPS signal is given as $F_{IMPS}(\omega) = \delta j(\omega)/e\delta I(\omega)$; *e* is a unit charge. For the IMVS method, the voltage response (δV) is measured and the frequency-dependent IMVS signal is given as $F_{IMVS}(\omega) = \delta V(\omega)/e\delta I(\omega)$. As shown in Figure 24, IMPS is performed under a short-circuit condition similar to that of TCD; information about electron diffusion is thus acquired. Alternatively, IMVS is performed at the open-circuit condition that provides the same kinetic information as obtained from the TVD method. The EIS method, in contrast, permits a simultaneous analysis of the impedance response to obtain information about electron transport and charge recombination at a specific *JV* point.

3.2. *Experiment*

(a) EIS method

Figure 25 shows a typical experiment for methods based on analysis of the frequency response of EIS and IMPS/IMVS measurements [111]. The instrument is generally operated with a potentiostat (PS) containing a built-in module as a frequency response

Downloaded by [National Chiao Tung University] at 06:29 21 November 2012

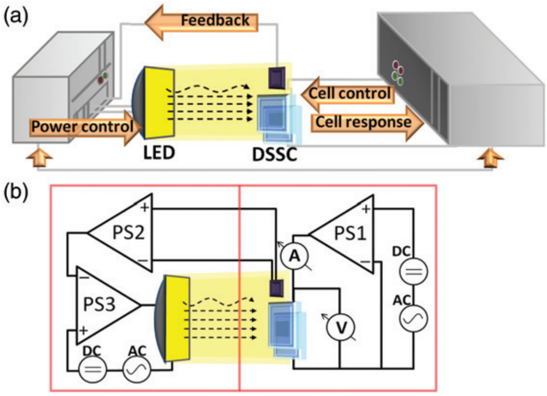

Figure 25. (Colour online) Experiment for frequency-domain measurements with EIS and IMPS/IMVS methods: (a) schematic representation of the instrument and (b) general circuit diagram of the apparatus. PS represents a potentiostat with a built-in frequency response analyser. The box on the right side is the master unit for EIS; the slave unit at the left side performs small-amplitude modulation of the light intensity for IMPS/IMVS.

analyzer (FRA); the stationary dc supply and signal response are controlled with a PS and the ac modulation and impedance response controlled with a FRA (PS1).

The amplitude of the modulated perturbation must be small to ensure that the impedance response of the system is linear; an amplitude from 5 to 10 mV is normally used in a EIS measurement for DSSC. A small perturbation is typically superimposed on a steady state such as a bias dc voltage or bias cw light during a frequency scan over a wide range. For DSSC measurements, a frequency range 10 mHz to 1 MHz is commonly chosen. The EIS measurements are classified into two types according to the performance conditions: a simple EIS approach and EIS with bias potentials and light intensities. In the simple EIS approach, the measurements are operated under an open-circuit condition in darkness or under illumination. In the other approach, EIS determinations are performed at a working point on the *J–V* curve of a device, under one sun illumination and a bias voltage in a range at least from 0 V to the open-circuit potential [19,20,107]. Another and similar approach is to operate under an open-circuit condition but to vary the intensity of the bias light [22,102]. In this method, a complete scan of frequency is achieved at each steady-state working point. To prevent systematic errors, the device must be stable during the entire measurements, and the response of the device must be related to the excitation signal and the desired condition only; any external variability such as temperature should be avoided.

(b) IMPS/IMVS methods

For measurements of IMPS and IMVS, a sinusoidal light perturbation with a small amplitude is applied over a frequency range. As shown in Figure 25, the measurements require another potentiostatic loop (PS2 and PS3 at the left side) for control of the intensity and modulation of the LED source. For more precise determination, an active feedback control of the intensity with PS2 from a photo-detector is added during

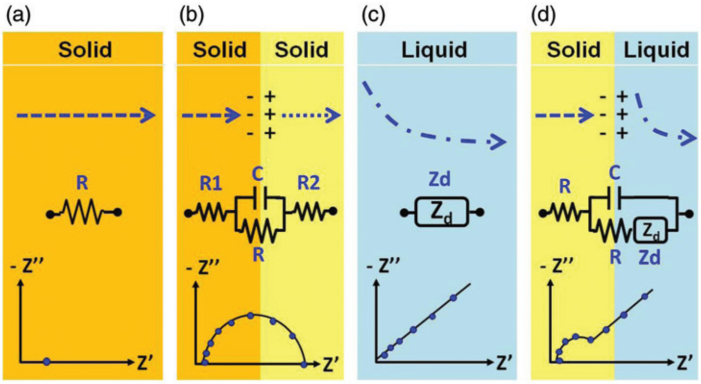

Figure 26. (Colour online) General equivalent circuits and relevant Nyquist plots in electrochemical systems for a (a) homogeneous solid phase, (b) solid/solid interface, (c) diffusion- controlled liquid system, and (d) solid/liquid interface.

the measurement. The LED light weakly absorbed by the dye molecules is driven by PS3 with the modulated light intensity much smaller than the cw bias light intensity. In the IMPS measurement, a photocurrent response is measured with PS1 involving the amplitude and the phase shift between the modulated light and the current response under a short-circuit condition. The IMVS measurements are operated with the same apparatus, but the photovoltage response is measured under an open-circuit condition.

3.3. *Data analysis*

(a) EIS method

For EIS, it is convenient to represent the impedance in terms of a complex notation, $Z(\omega) = Z_{\text{Re}} + iZ_{\text{Im}}$ or $Z(\omega) = Z' + iZ''$. The component along the y axis is the imaginary part that is multiplied by $i \equiv \sqrt{-1} \equiv \exp(i\pi/2)$. The EIS results are displayed in plots of various types. For a Nyquist plot, a complex plane of the imaginary part against the real part of the impedance is plotted for various values of frequency. For a Bode plot, both impedance modulus and phase angle (log |Z| and ϕ) are alternatively plotted as a function of logarithmic frequency.

Figure 26 shows an idealised electrical equivalent circuit for various interfaces. The impedance for a homogeneous distribution system such as a bulk solid or an electrolyte is represented with a pure resistance (Figure 26a); the behavior follows Ohm's law, and the phase angle is zero, resulting in a zero slope in a Bode plot and the real part in a Nyquist plot [112,113]. In contrast, a pure capacitance shows a phase angle $\pi/2$ and a slope -1 in a Bode plot, and represents the imaginary part of the impedance. Figure 26(b) shows a *RC* circuit to represent a solid-solid interface that gives a semicircle in a Nyquist plot. In general, a complex circuit model comprising resistance, capacitance, Warburg-impedance and a constant phase element (CPE) in series or in parallel is more appropriate to represent an interface of a device; for example, an electrolyte in which the microscopic

Downloaded by [National Chiao Tung University] at 06:29 21 November 2012

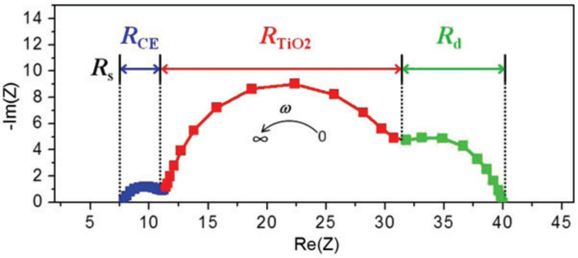

Figure 27. (Colour online) A typical impedance spectrum (Nyquist plot) of a dye-sensitised solar cell showing the three major semicircles arisen from a frequency scan of the ac potential.

properties are distributed could lead to a non-linear conducting mechanism. Under these conditions, a Warburg diffusion impedance (Z_d) considering mass transport serves to describe the electric response of the diffusion-controlled system instead of ideal circuit elements that are inadequate because of an independence of frequency. According to the literature [14,113,114], Z_d is proportional to $\omega^{-1/2}$ resulting in a phase angle about 45° and slope $-(1/2)$ in a phase diagram and represented as a straight line with unit slope in the complex impedance plot, shown in Figure 26(c). Figure 26(d) shows an electrochemical system that occurs at an interface of a solution and an electrode; the impedance is represented with a faradaic current and a double layer charging near the electrode surface as a parallel *RC* circuit. A semicircle combined with a straight line is thus obtained in the complex plot.

A typical impedance spectrum of a DSSC reveals three semicircles on the Nyquist plot shown in Figure 27. The offset on the real part represents the ohmic series resistance (R_s) of the cell including the resistance of the substrates, electrolyte, electrical contact and wiring of a device. According to the time constants of the different impedance components in a DSSC, the separated semicircles are shown in the complex plane following the related characteristic frequency range in which the arcs at high frequency (kHz), middle frequency (1–10 Hz) and low frequency (0.01–1 Hz) correspond to the redox reaction at the counter electrode (R_{CE}), electron transfer at the nanoporous photoelectrode (R_{TiO2}) and diffusion within the electrolyte (R_d), respectively.

On fitting the spectrum with an appropriate equivalent circuit, it is capable of identifying and extracting the electrical elements of the circuit. A proper equivalent circuit represents the pertinent physical processes in the determined system. Figure 28 shows the basic equivalent circuit used to model a DSSC on the basis of the transmission line model [33,114,115]. The equivalent circuit elements characterise the series resistance (R_s), electron transport resistance in the TiO_2 matrix (R_{tr}), charge transfer resistance related to recombination (R_{rec}) and chemical capacitance (C_μ) at the TiO_2/electrolyte interface. For thickness L of the TiO_2 film, the total transport resistance is $R_{tr} = r_{tr}\ L$; the total recombination resistance is $R_{rec} = r_{rec}/L$ and the total capacitance is $C_\mu = c_\mu L$. A parallel *RC* circuit refers to the charge-transfer resistance (R_{TCO}), and the double-layer capacitance (C_{TCO}) at the transparent conducting oxide (TCO) substrate/electrolyte interface is added. The diffusion impedance of the redox couple species in the electrolyte is represented by Z_d; the charge transfer at the counter electrode is described by a parallel *RC* circuit composed

Downloaded by [National Chiao Tung University] at 06:29 21 November 2012

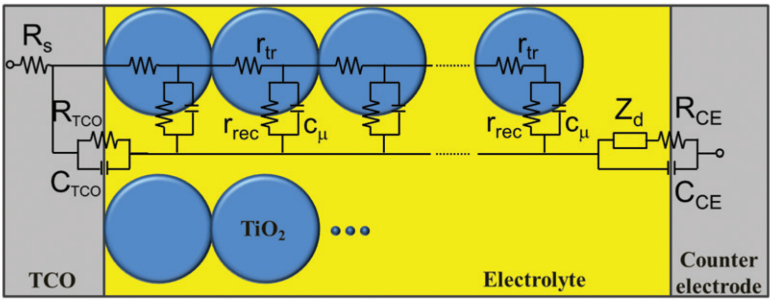

Figure 28. (Colour online) Equivalent circuit model for a dye-sensitised solar cell.

Downloaded by [National Chiao Tung University] at 06:29 21 November 2012

of resistance (R_{CE}) and capacitance (C_{CE}). It is convenient to fit the impedance spectrum with commercial software such as ZView [116] with the equivalent circuit in Figure 28 for a precise simulation.

Following the diffusion-recombination model, the electron transport through the TiO_2 layer is determined as R_{tr} and described with a trapping/detrapping model [117]; the recombination behavior affected by the intrinsic nature of a sensitiser, additives in the electrolyte or the morphology of the TiO_2 mesoporous layer, and so forth, are described with R_{rec} [118–120]. In the case of rapid electron transport, $R_{tr} < R_{rec}$, the total resistance of TiO_2 becomes approximated as $R_{TiO_2} = 1/3R_{tr} + R_{rec}$; the impedance spectrum reveals a straight line concerning the Warburg impedance in the high-frequency range, followed by a semicircle at low frequency [20]. Contrary to a transmission-line impedance, a device exhibiting large recombination, $R_{tr} > R_{rec}$, becomes the Gerischer impedance; the total resistance of TiO_2 is expressed as $R_{TiO_2} = (R_{tr}\ R_{rec})^{1/2}$, which shows a long diffusion line and a distorted arc in the EIS spectrum. Chemical capacitance C_μ denotes the impedance of charge accumulation in TiO_2 governed by the density of electronic states. In most devices, the impedance results show a slightly depressed semicircle revealing an imperfect capacitance. For more precise analysis, the capacitor elements become replaced with a CPE describing a non-uniform distribution of current in the TiO_2 matrix. In relation to the recombination and transport properties, the electron lifetimes (τ_R) are represented with $\tau_R = R_{rec}\ C_\mu$, the electron diffusion coefficient (D) is expressed as $D = L^2/R_{tr}C_\mu$, and the effective electron-diffusion length (L_n) is related to the recombination and transport resistances via $L_n = L\sqrt{R_{rec}/R_{tr}}$ [19,20]. As commercial systems are available for the EIS measurements, the EIS data are easily acquired, but analysis and interpretation of the data with an appropriate model become a challenging task. To elucidate the underlying mechanisms related to the cell performance, an example is given in the next section with the EIS experiments performed under varied bias potentials.

(b) IMPS/IMVS methods

Figure 29(a) and (b) shows typical IMPS and IMVS responses obtained for a short circuit and an open circuit, respectively, under the condition with a constant bias irradiation. For IMVS (Figure 29b), a nearly perfect semicircle appears in the lower complex plane of the IMVS spectrum (the negative imaginary component of the IMVS response was inverted for the plots shown in Figure 29b) because the photovoltage

Downloaded by [National Chiao Tung University] at 06:29 21 November 2012

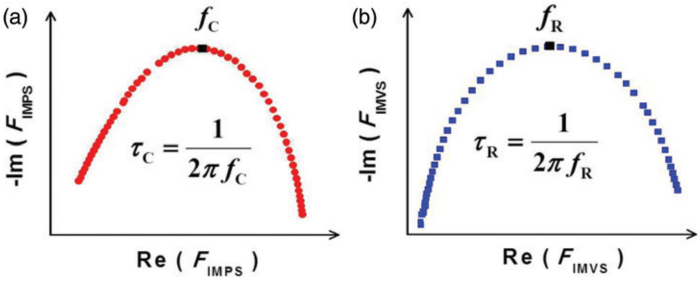

Figure 29. (Colour online) Plots of Nyquist type showing (a) IMPS and (b) IMVS responses. The negative imaginary components in the lower complex plane of both plots are inverted for a conventional visualisation.

response lags behind the illumination. For IMPS (Figure 29a), the current response also locates in the lower complex plane for the same reason as for IMVS, but a perfect semicircle is not observed in the IMPS plot. The shape of the IMPS plot always shows a distorted arc or a semicircle with a linear part at high frequency range due to the effect of *RC* attenuation in the high-frequency region [14,21] or unhomogeneous light absorption in the film [31,110]. The collection time (τ_C) characterising the electron transport to the anode under the short-circuit condition is related to the minimum-point angular frequency, $\omega_{min} = 2\pi f_C$, according to the following expression,

$$\tau_C = \left(\frac{1}{\omega_{min}}\right)_{SC} = \frac{1}{2\pi f_C} \tag{14}$$

in which f_C is the minimum-point frequency (in Hz) of the IMPS response. The electron lifetime (τ_R) characterising the charge recombination at the TiO_2/electrolyte interface under the open-circuit condition is similarly determined by the angular frequency at the minimum of the semicircle via the following expression,

$$\tau_R = \left(\frac{1}{\omega_{min}}\right)_{OC} = \frac{1}{2\pi f_R} \tag{15}$$

in which f_R is the minimum-point frequency (in Hz) of the IMVS response.

3.4. *Examples of techniques in the frequency domain*

The frequency-domain techniques introduced herein have been extensively applied for the applications of DSSC. For example, the IMPS/IMVS methods were applied to various systems such as Ru complexes [121–123], organic dyes [124,125], liquid electrolytes [49,74,126–129], quasi-solid [130,131] and solid-state electrolytes [132–134], TiO_2 and doped TiO_2 nanostructures [135–151], and ZnO/TiO_2 composite nanomaterials [152–154]. In the following, we provide five examples how EIS and the IMPS/IMVS methods are applied to understand the kinetics of transport and recombination in relation to the corresponding device performance: (a) DSSC made of TiO_2 nanotube arrays (TNT)

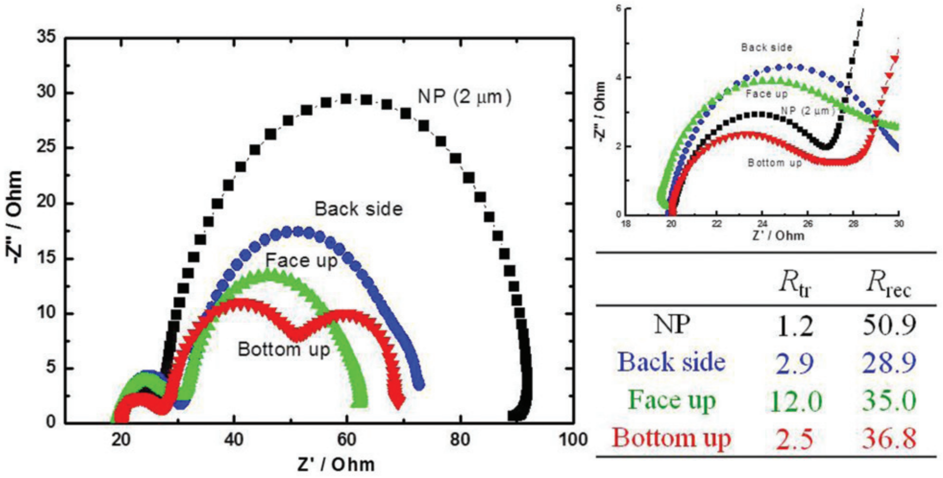

	R_{tr}	R_{rec}
NP	1.2	50.9
Back side	2.9	28.9
Face up	12.0	35.0
Bottom up	2.5	36.8

Figure 30. (Colour online) Nyquist plots obtained from electrochemical impedance spectra (EIS) measured for corresponding DSSC devices under AM-1.5 illumination and an open-circuit condition [155]. Reproduced by permission of The Royal Society of Chemistry.

according to a simple EIS approach [155], (b) porphyrin-sensitised solar cells with EIS and varied bias potentials and light illumination [156], (c) Ru-based devices with CE and IMVS methods [97], (d) co-sensitisation of porphyrin with organic dye with CE/IMVS methods [157] and (e) DSSC made of HD and NP TiO_2 films studied with CE and IMPS/IMVS methods [158].

(a) Simple EIS approach

The easiest way to extract information about the transport and recombination to understand the performance of a DSSC device from is to perform the impedance measurement with only one frequency scan (simple EIS approach), but a correct interpretation of the EIS data relies on a careful analysis based on modeling with an appropriate equivalent circuit. The simple EIS approach works when the impedance response is sensitive to the variation of an interfacial property that varies with a material. Simple EIS investigations of organic dyes [23,119], Ru-based photosensitisers [39], additives in an electrolyte [159], a gel-type electrolyte [118] and TiO_2 nanostructures [160–163] are reported. Here we introduce how this simple EIS approach is applied to rationalise the photovoltaic performance for devices fabricated with TNT photoanodes.

TNT, as vertically oriented arrays and prepared using potentiostatic anodisation, are regarded as a promising photoanode in DSSC applications [164]. A traditional TNT-DSSC device based on illumination of the back side suffers a degradation of performance due to light absorption by the iodide/tri-iodide electrolyte and the Pt-coated counter electrode. To improve the cell performance for a NT-DSSC device, transparent nanotube arrays were fabricated on a substrate of transparent conducting oxide (TCO) with various methods [165–167]. The devices fabricated based on a conventional upright (face up)

Downloaded by [National Chiao Tung University] at 06:29 21 November 2012

Downloaded by [National Chiao Tung University] at 06:29 21 November 2012

transfer exhibit much poorer performance than with the inverted (bottom up) approach ($\eta = 4.84\%$ vs. 6.24%), indicating that cracks at the interface of TNT arrays might hinder electron transport across the interface. To explain how the interfacial problems affect the device performances, simple EIS measurements were performed; the results and data analysis are shown in Figure 30 [155].

The impedance results were fitted according to the equivalent circuits shown in Figure 28. The equivalent circuit elements describe the electron transport in a DSSC with typical physical meaning introduced earlier. The transport resistances $R_{tr}/\Omega\,\text{cm}^2$ at the TiO_2/substrate interface are 1.2, 2.9, 12.0 and 2.5 for DSSC devices based on NP, TNT, face-up and bottom-up structures, respectively. The NP-only device has a small R_{tr} value because of its thin-film nature ($L = 2\,\mu\text{m}$). The transport resistance of the bottom-up transferred film is slightly smaller than that of the TNT film as prepared without film transfer; the face-up attached TNT-DSSC device shows the largest transport resistance, indicating that electron diffusion was hindered by the cracks and gaps at the TNT/NP interface. This result is consistent with the observed cell performance in that a smaller current density at short circuit was observed for the face-up device than for the bottom-up device, which is attributed to the larger R_{tr} with similar R_{rec} for the former than for the latter, giving the lower charge-collection efficiency for the face-up device. These results thus provide solid evidence for the transfer of bottom-up TNT arrays on a NP-coated TCO substrate to make a highly efficient TNT-DSSC device with transparent front-side illumination [155].

(b) EIS with varied bias potential

As noted above, EIS measured with varied bias potential provide the characteristics of transport resistance, recombination resistance and chemical capacitance dependent on voltage. For the EIS experiments performed with open circuit and varied light intensity, the impedance parameters related to kinetic processes depend on V_{OC}. The influence of the recombination and the conduction band edge can be established under this condition [168–172]. For example, Wang and co-workers outlined the significance of impedance spectra under varied light intensity to understand the effect of aging and the influences of sensitisers [170] and photoanodes [173]. The experiments performed with varied bias potentials in darkness [6,33,41,70,174–181] or under illumination provide kinetic information related to the dark current and the JV curve, respectively. Under such conditions, various systems such as organic dyes [182], porphyrin sensitisers [183,184], quantum dots [185–187], solid-state electrolytes [188] and metal oxide nanostructures [180,189–191] were studied.

The significance of porphyrin-sensitised solar cells is introduced in the preceding section. Here an example is given for porphyrin sensitisers investigated with a complete EIS analysis with varied bias potential [156]. Three porphyrin sensitisers (YD20-YD22, Figure 31) were investigated based on the structure of YD2-oC8 but with extended π-conjugation to enhance the light-harvesting ability. These porphyrin dyes were fabricated into DSSC devices for photovoltaic and detailed EIS characterisation. The photovoltaic results indicate that the values of J_{SC} exhibit a trend YD20 > YD22 > YD21; the values of V_{OC} display a trend YD20 > YD22 ~ YD21; the overall power conversion efficiencies (η) show the same order as J_{SC}, consistent with the variations of the IPCE action spectra showing the same order. As a result, YD20 has the greatest J_{SC} ($17.43\,\text{mA cm}^{-2}$) and V_{OC}

Downloaded by [National Chiao Tung University] at 06:29 21 November 2012

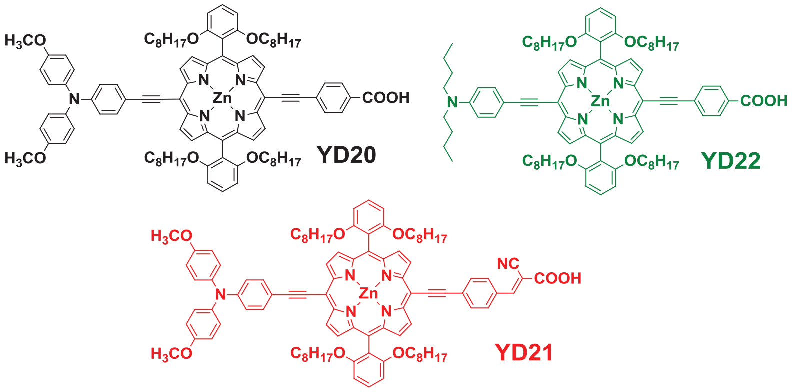

Figure 31. (Colour online) Molecular structures of three porphyrin dyes, YD20, YD21 and YD22 [156].

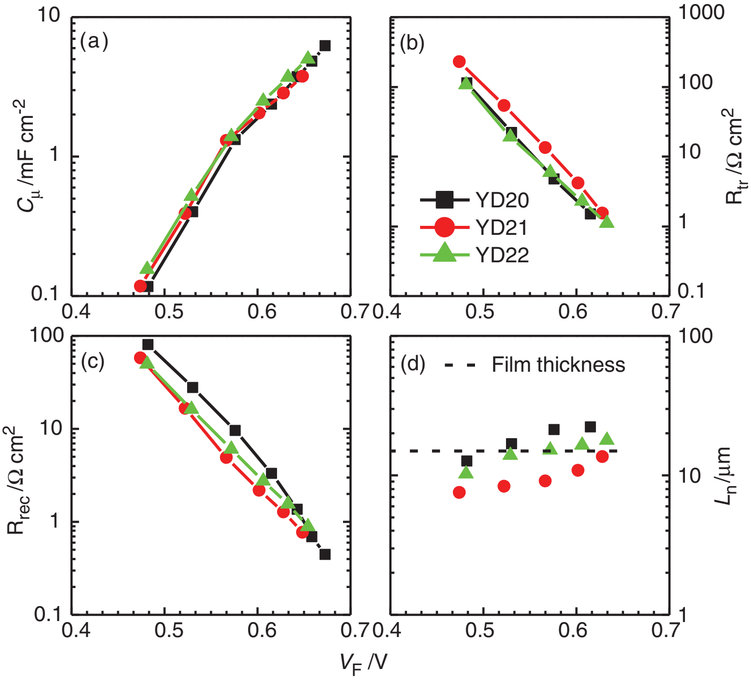

Figure 32. (a) Capacitance, (b) transport resistance, (c) recombination resistance, and (d) diffusion length of YD20-YD22 dyes in DSSC plotted with respect to the Fermi level voltage (V_F) on removal of the effect of series resistance [156]. Reproduced by permission of The Royal Society of Chemistry.

(676 mV), so yields the greatest η (8.1%) among these three porphyrins under investigation.

From a fit of impedance spectra of DSSC at varied applied potentials between 0 and 0.75 V under one sun illumination, the resulting chemical capacitance (C_μ), transport

Downloaded by [National Chiao Tung University] at 06:29 21 November 2012

resistance in the TiO_2 (R_{tr}), recombination resistance (R_{rec}) are shown as a function of the Fermi level (V_F) in Figure 32(a–c), respectively. Other contributions to the total resistance of the cell such as diffusion, counter electrode and FTO resistances were grouped as series resistance (R_S). The effect of R_S in the applied potential (V_{app}) was removed to obtain V_F; that may be calculated through $V_F = V_{app} - jR_S$. From the plot of C_μ vs. V_F shown in Figure 32(a), the position of the conduction band edge of TiO_2 (E_c) is estimated. Data from transport resistance shown in Figure 32(b) provide small displacements in E_c, indicating that all TiO_2 conduction bands remain almost unchanged for those three dyes, as obtained from the capacitance data. To understand the origin of the small differences in V_{OC} found for the three dyes one must analyse the behaviour of the recombination resistance in Figure 32(c). The results indicate that YD20 has a larger recombination resistance and V_{OC}, whereas YD21 and YD22 have similar values of R_{rec} showing almost the same V_{OC}, consistent with other work [20,182,183] showing that the greater is the value of R_{rec}, the larger is V_{OC}, but only large changes of photocurrent produce small variations of V_{OC}.

Data from R_{rec} and R_{tr} are usable to calculate the diffusion length ($L_n = L\sqrt{R_{rec}/R_{tr}}$) in a TiO_2 film shown in Figure 32(d); the film thickness L is indicated as a dashed line. Values of L_n exhibit a systematic trend with the order YD20 > YD22 > YD21; those of YD20 and YD22 attain values greater than their film thickness, whereas those of YD21 are significantly smaller than the film thickness. This result implies that the YD21 device suffers from a poorer collection efficiency of injected electrons so to produce an extra decrease of J_{SC} found for this device.

The small differences found for the position of the conduction band edge (E_c) might assist also to refine the roles of the link in these three porphyrin dyes. If the Fermi level potential is shifted the amounts found for the displacement of E_c, it is possible to compare the recombination resistance of the devices at the potential level with the same number of injected electrons. A similar approach was introduced previously in temporally resolved investigations, as shown in Figures 13(b) and 21(b), to compare the recombination times of systems at the same conduction-band edge level. Here we define the potential at the equivalent conduction-band position as $V_{ecb} = V_F - \Delta E_c/e$; e is the electron charge and $\Delta E_c = E_c - E_{c,\ ref}$, for which $E_{c,\ ref}$ is the position of the conduction band of YD20 serving as a reference. Based on these conditions, we transfer Figure 32(a–c) into Figure 33(a–c), which show C_μ (a), R_{tr} (b), and R_{rec} (c) as a function of V_{ecb}. Although the chemical capacitance (Figure 33a) and the transport resistance (Figure 33b) of the three dyes match quite well, the recombination resistance (Figure 33c) of the YD21 device is much smaller than those of the YD20 and YD22 devices. These results allow us this conclusion: relative to the YD20 device, the smaller V_{OC} of YD22 was due to a small shift of the conduction band, but the smaller V_{OC} of YD21 was due to a significant charge recombination. From the structural viewpoint, the use of floppy cyanoacrylic acid as acceptor and anchoring group in YD21 might provide more free space (decreased dye-loading) for rapid charge recombination to occur than the use of the rigid ethynylbenzoic acid in YD20 and YD22 [156].

(c) Ru dyes

We introduced the kinetics of transport and recombination based on transient photoelectric measurements for devices made of three fluoro-substituted heteroleptic ruthenium dyes (RD5, RD12 and RD15, Figure 14). Because the shifts of the TiO_2 conduction band edge potentials and electron lifetimes (τ_R) play important roles in the

Downloaded by [National Chiao Tung University] at 06:29 21 November 2012

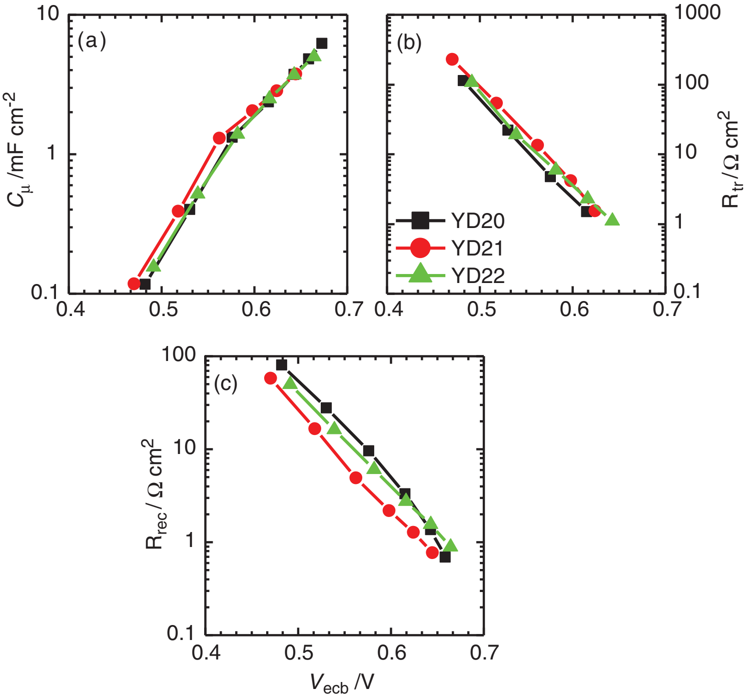

Figure 33. (Colour online) (a) Capacitance, (b) transport resistance and (c) recombination resistance of dyes **YD20-YD22** in DSSC plotted with respect to the equivalent common conduction band voltage (V_{ecb}) [156]. Reproduced by permission of The Royal Society of Chemistry.

device performance, in particular to affect the values of V_{OC}, in this section we compare those properties for the same systems based on the CE and IMVS measurements using the CIMPS equipment (Zahner) under an open-circuit condition. Figure 34(a) displays plots of V_{OC} vs. N_e for the four systems (N719 served as a reference) at five intensities ($1.5-30\,\mathrm{mW\,cm^{-2}}$) of red light from a LED probe ($\lambda = 610\,\mathrm{nm}$) [97]. The CE results indicate that the TiO_2 conduction band edge potentials of the devices show a systematic upward shift with order N719 > RD15 > RD12 > RD5, consistent with the time-domain results (Figure 16), but the shifts have a smaller extent, accounting for the variation of their V_{OC}. Increased substitution of fluorine atoms on the phenyl group hence shifts the potential of the conduction-band edge of TiO_2 towards a more negative direction (upward shift). These observations might thus indicate that a fluoro-substituted ligand would produce a dipole moment with the negative partial charge pointing toward the TiO_2 surface to raise the potential [192].

Figure 34(b) shows plots of τ_R vs. N_e for four systems at five light intensities [97]. The results indicate a systematic trend with electron lifetime (corresponding to the degree of charge recombination) showing the order RD15 > RD12 > RD5, consistent with the variation of V_{OC} showing the same order for the fluoro-substituted devices. The electron lifetime of the N719 device is the smallest in the series, indicating that an incorporation of benzimidazole ligands in the RD series of dyes effectively retards the charge recombination between the CB electrons on the TiO_2 surface and the I_3^- species in the electrolyte. The

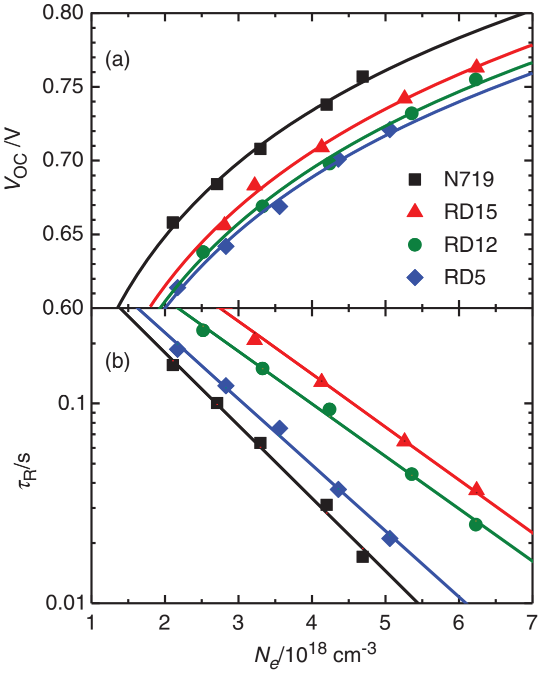

Figure 34. (Colour online) (a) Open-circuit voltage (V_{OC}) and (b) electron lifetime (τ_R) as a function of charge density (N_e) for devices made of RD5, RD12, RD15 and N719 under five bias irradiations [97]. Reprinted with permission from J. Phys. Chem. Lett. 3, 1830 (2012). Copyright 2012 American Chemical Society.

plots of τ_R vs. N_e shown in Figure 17 display the order RD12 > RD15 > RD5. The results obtained from the TVD and IMVS measurements show a similar trend for plots of τ_R vs. V_{OC}, and the discrepancy involved in the plots of τ_R vs. N_e between the two measurements is due to the corrections for the potential shifts from the CE measurements. The charge recombination rates between the RD12 and RD15 devices are hence expected to be similar, with the same conclusions as made previously. We emphasise that the benzimidazole ligands in Ru dyes of this series have the effect of retarding the charge recombination but also leading to a downward shift of the TiO_2 conduction band edge potential relative to that of the N719 device.

(d) Co-sensitisation

Co-sensitisation of two or more dyes with complementary absorption spectra on a TiO_2 film is a well-known strategy to enhance the light-harvesting ability for DSSC. An example is given below of how IMVS measurements explain the enhanced photovoltaic performance for devices made of a porphyrin dye (LD12) [64] co-sensitised with an organic dye (CD5) [193]. Both J_{SC} and V_{OC} of the co-sensitised devices were significantly enhanced relative to their corresponding single-dye sensitised devices, improving the overall performance for the LD12 + CD5 device ($\eta = 9.0\%$) by 20% and 58% with respect to devices LD12 ($\eta = 7.5\%$) and CD5 ($\eta = 5.7\%$), respectively [157].

Downloaded by [National Chiao Tung University] at 06:29 21 November 2012

Downloaded by [National Chiao Tung University] at 06:29 21 November 2012

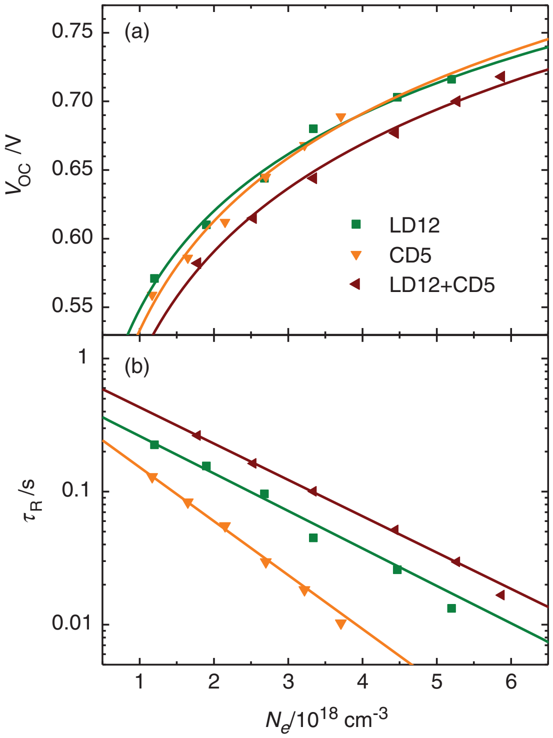

Figure 35. (Colour online) (a) Open-circuit voltage (V_{OC}) and (b) electron lifetimes (τ_R) as a function of charge density (N_e) for the devices made of LD12 along, CD5 alone and their co-sensitized combination under six bias light irradiations [157]. Reproduced by permission of The Royal Society of Chemistry.

Figure 35(a) displays plots of V_{OC} vs. N_e for the three systems at six intensities of white light from a LED. The CE results indicate that the TiO_2 conduction band edge potentials of the LD12 and CD5 devices are similar to each other, but that of the LD12 + CD5 device exhibits a potential shift down ~25 mV with respect to the individual dye-sensitised devices. Co-sensitisation of LD12 with CD5 on TiO_2 film thus has the effect of lowering the TiO_2 conduction band edge potential, but the potential down-shift of the co-sensitisation system in this case gives a wrong direction to account for the observed V_{OC} enhancement for the LD12 + CD5 system, for which IMVS measurements were performed to obtain kinetic information about the charge recombination.

Figure 35(b) shows plots of τ_R vs. N_e for the three systems at six light intensities. The results indicate a systematic trend with electron lifetimes (corresponding to the degree of charge recombination) showing order LD12 + CD5 > LD12 > CD5, consistent with the variation of V_{OC} in the same order. These results are consistent with those of the black dye + Y1 co-sensitisation system showing an increase ~20 mV in V_{OC}, which is also explicable according to the electron lifetimes increased upon co-sensitisation [194]. For the TT1 + D2 co-sensitisation system, these observed lifetimes in the co-sensitised device are between those of the D2 and the TT1 devices, correlating well with the trend of V_{OC} [195].

Downloaded by [National Chiao Tung University] at 06:29 21 November 2012

Based on the cobalt redox electrolyte, the decreased V_{OC} of the YD2-oC8 + Y123 device relative to that of the device containing only the YD2-oC8 dye is also explicable by the smaller electron lifetimes for the former than for the latter [9]. For the LD12 + CD5 system, the observed V_{OC} becomes enhanced upon co-sensitisation of LD12 with CD5 due to the effect of a retarded charge recombination even though the potential of TiO_2 shifted slightly down. Such a retardation was rationalised for an effective combination between zinc porphyrin with long alkoxyl chains and the organic dye with bulky spiral *cis*-stilbene/fluorene hybrids, such that they formed a compact layer on the surface of TiO_2 to impede the approach of triiodide anions in the electrolyte to the TiO_2 surface [91,157].

(e) Titania

The last example in this review serves for a comparison for experimental approaches of the two types, time domain (TCD/TVD) and frequency domain (IMPS/IMVS), and to rationalise the properties of transport and recombination for the devices made of NP and HD films (Figure 18). The NP and HD devices made of thin TiO_2 films ($L \sim 10\,\mu m$) were applied for the IMPS/IMVS measurements under five bias irradiations (power densities I_0 in the range $1.1-23\,mW\,cm^{-2}$) using the CIMPS system developed by Zahner. A red LED ($\lambda = 610\,nm$) served as the bias lamp for which $< 10\%$ of the bias light intensity was modulated to give an ac signal as a perturbation of small amplitude for the IMPS and IMVS measurements under the short-circuit and open-circuit conditions, respectively.

Figure 36(a) and (b) shows plots of τ_C and τ_R, respectively, as a function of bias photon flux obtained from the IMPS and IMVS measurements. The results resemble those of the TCD/TVD results (Figure 19), showing that the values of τ_C are smaller for the HD film than for the NP film, whereas the values of τ_R are almost identical for both films. Figure 37(a) and (b) shows plots of D vs. J_{SC} and τ_R vs. V_{OC} obtained from the IMPS and IMVS measurements, respectively. The results shown in Figure 37 again exhibit the feature for the kinetics of transport and recombination the same as those shown in Figure 21: the electron transport in the HD film was much more rapid than in the NP film compared at the same photocurrent level whereas the charge recombination rate in the HD film was slower than in the NP film compared at the same photovoltage level. Under the same bias intensities, the values of J_{SC} of HD were slightly larger than those of NP; this photovoltaic feature is similar to the results shown in Figures 18(a) and 21(a). The values of V_{OC} of HD are larger by $\sim 20\,mV$ than those of NP under the same bias red irradiations (Figure 37b), but the discrepancy in V_{OC} was only $\sim 5\,mV$ under the same bias white irradiations (Figures 18b and 21b), because of the varied thickness of the TiO_2 films for measurements of the two types.

Because V_{OC} differs for the two devices measured under the same bias intensity, the difference of the potential shift is crucial to compare the kinetics of charge recombination at the same Fermi level position of injected electrons. Figure 38(a) shows plots of V_{OC} vs. N_e for the two devices, indicating that the HD potential locates above the NP potential by $\sim 10\,mV$ at large charge densities whereas the two potentials are almost the same at small charge densities. As the potentials of the two devices are similar, the values of τ_R of the HD device are still larger than those of the NP device when both are compared at the same N_e (Figure 38b). The slight deviation observed in V_{OC} might hence be due to the retarded

Downloaded by [National Chiao Tung University] at 06:29 21 November 2012

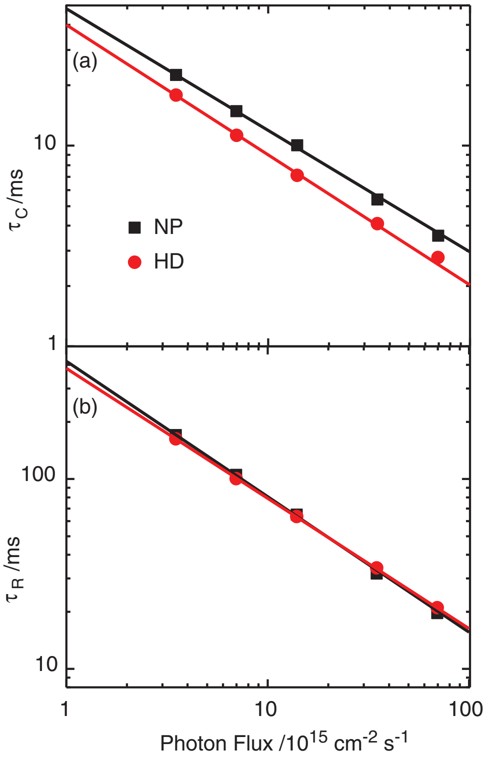

Figure 36. (Colour online) Logarithmic plots of (a) electron collection time (τ_C) and (b) electron lifetime (τ_R) as a function of bias photon flux from a red LED ($\lambda = 610$ nm) at five intensities (1.1–23 mW cm^{-2}) for devices made of NP and HD TiO_2 films. τ_C and τ_R were determined from the IMPS and IMVS measurements, respectively [158].

charge recombination of the HD device relative to the NP device. The electron diffusion in the HD film is much more rapid than in the NP film, which led to much greater efficiencies of charge collection for HD than for NP; the same conclusion we drew from results obtained from the TCD measurements.

4. Concluding remarks

In this review, we emphasise the kinetic essences of dye-sensitised solar cells and the experimental strategies to relate the photovoltaic performance of the device to the properties electron transport and charge recombination based on perturbation probes of small amplitude superimposed on large cw bias irradiations and large dc bias potentials using either temporally resolved or frequency-domain techniques. For the temporally resolved methods, the temporal profiles of transient photocurrent decays (TCD) and those of transient photovoltage decays (TVD) were obtained under short-circuit and open-circuit conditions, respectively; the kinetics in devices related to the electron transport at a short circuit or the charge recombination at an open circuit can accordingly be understood

Downloaded by [National Chiao Tung University] at 06:29 21 November 2012

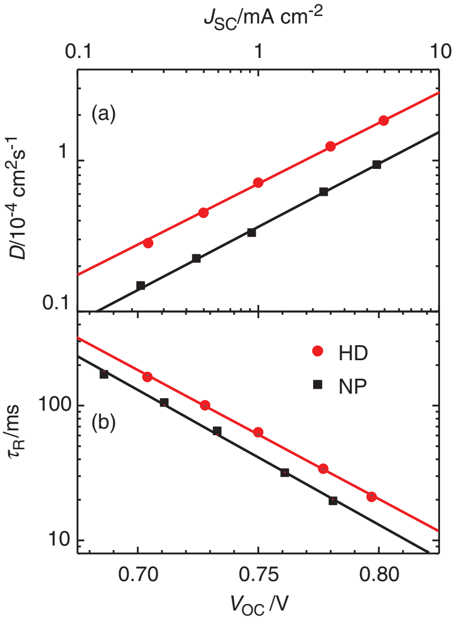

Figure 37. (Colour online) (a) Logarithmic plots of diffusion coefficient (D) vs. J_{SC} and (b) semi-logarithmic plots of recombination time (τ_R) vs. V_{OC} for devices fabricated with HD and NP films under bias irradiations of five intensities obtained from IMPS and IMVS measurements, respectively. D was determined according to Equation (6) with TiO_2 film thickness $L = 10\,\mu m$ [158].

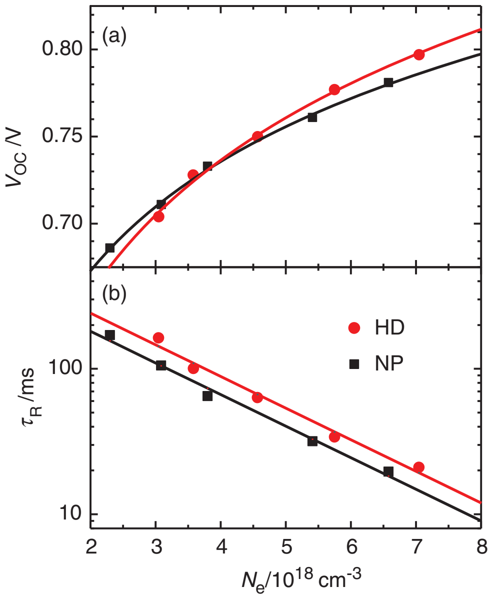

Figure 38. (Colour online) (a) Open-circuit voltage (V_{OC}) and (b) electron lifetimes (τ_R) as a function of charge density (N_e) for the devices fabricated using the HD and NP films under five bias light irradiations. The results were obtained from CE and IMVS measurements [158].

Downloaded by [National Chiao Tung University] at 06:29 21 November 2012

in an intuitive manner. For the frequency-domain methods such as involving electrochemical impedance spectroscopy (EIS), the data are readily acquired, but analysis and interpretation of the EIS data might prove challenging. The reason for the complication of the EIS approach is its intrinsic nature using an ac potential probe, which is electrically responsive to any interface existing in the device. To simplify such complication, the small portion of the cw bias irradiation has its intensity modulated to serve as the 'ac probe'; the current response is monitored at a short circuit (IMPS) or the voltage response is monitored at an open circuit (IMVS). In such a way, the key interfacial properties of the photoanode sensitive to irradiation give electric responses from the measurements; the kinetic information obtained from the IMPS/IMVS methods in the frequency domain are in principle equivalent to those obtained from the TCD/TVD methods in the time domain. The determination of the electron transport time or the electron lifetime relies, however, on only the minimum-point frequency, which is a simple approach as for IMVS, but it might become problematic if the response becomes complicated, as is typically the case for IMPS. Since the time and frequency domain responses correlate to each other through Fourier transform, the same problem might also involve for the TCD method when the transients exhibit a multiple exponential decay feature.

In terms of time consumed in collection of the data, the TCD/TVD methods introduced herein are preferable if the corresponding transport kinetics are not rapid (the time resolution using LED sources is about 1 μs); the data acquisition of IMVS for a slow recombination rate might be tedious and thus unreliable. Because the charge-extraction (CE) method provides important information about the potential shift and provides a reference for comparison of the recombination kinetics, a combination of the CE and TCD/TVD measurements would provide sufficient information to understand the interfacial properties of the anode in DSSC. However, the kinetic information obtained using the TCD/TVD or the IMPS/IMVS methods are limited to two extreme conditions. The EIS measurements, on the other hand, can be made along the *JV* curve to acquire further information not only for the photoanode but also for the electrolyte and counter electrode.

In this review we provide case studies for various DSSC systems using either a temporally resolved or a frequency-domain approach to understand the operating principle of the device and to highlight the applicability of those techniques with respect to the device performance from an experimental point of view. The articles cited and discussed here aim to provide an appropriate kinetic model to support or to rationalise the photovoltaic performance of the device, to guide the design of new materials to boost the cell efficiencies in the near future. There are many other fundamental issues for further review and discussion, such as the trapping and de-trapping model, the empirical non-ideality factor, the DOS distribution and the characteristic energy; these properties depend strongly on the system under investigation. Within this review, we focus our attention on photoelectric responses of DSSC devices and neglected temporally resolved spectrometric techniques, such as femtosecond fluorescence decays and transient absorption kinetics, which have been broadly applied on thin-film samples to acquire dynamical information on the interfacial electron injection between a dye and TiO_2. We encourage work on theoretical simulations both at the device structural level and at the molecular level, to enhance the understanding of this complicated solar system.

Downloaded by [National Chiao Tung University] at 06:29 21 November 2012

Acknowledgements

We thank Dr Liyang Luo for his contribution on setup of an initial laser-induced transient photoelectric system in our group. We are indebted to our collaborators, Prof. Chen-Yu Yeh of NCHU (Taiwan), Prof. Ching-Yao Lin of NCNU (Taiwan) and Prof. Chen-Hsiung Hung of Academia Sinica (Taiwan), who provided invaluable porphyrin dyes for transient photoelectric or impedance spectral characterisations reported in this review article. We are grateful to Prof. Juan Bisquert of UJI (Spain) and Prof. Janne Halme of Aatto University (Finland) for many enlightening discussions on impedance spectroscopy and constructive suggestions for this report. We thank the researchers for their works cited in this review. National Science Council of Taiwan and Ministry of Education of Taiwan, under the ATU program, provided support for this project.

References

[1] M. K. Nazeeruddin, A. Kay, I. Rodicio, R. Humphry-Baker, E. Mueller, P. Liska, N. Vlachopoulos, and M. Graetzel, J. Am. Chem. Soc. **115**, 6382 (1993).
[2] M. Grätzel, Acc. Chem. Res. **42**, 1788 (2009).
[3] A. Hagfeldt, G. Boschloo, L. Sun, L. Kloo, and H. Pettersson, Chem. Rev. **110**, 6595 (2010).
[4] T. W. Hamann, R. A. Jensen, A. B. F. Martinson, H. Van Ryswyk, and J. T. Hupp, Energy Environ. Sci. **1**, 66 (2008).
[5] A. B. F. Martinson, T. W. Hamann, M. J. Pellin, and J. T. Hupp, Chem. Eur. J. **14**, 4458 (2008).
[6] C.-Y. Chen, M. Wang, J.-Y. Li, N. Pootrakulchote, L. Alibabaei, C.-h. Ngoc-le, J.-D. Decoppet, J.-H. Tsai, C. Graützel, C.-G. Wu, S. M. Zakeeruddin, and M. Graützel, ACS Nano **3**, 3103 (2009).
[7] Y. Cao, Y. Bai, Q. Yu, Y. Cheng, S. Liu, D. Shi, F. Gao, and P. Wang, J. Phys. Chem. C **113**, 6290 (2009).
[8] Q. Yu, Y. Wang, Z. Yi, N. Zu, J. Zhang, M. Zhang, and P. Wang, ACS Nano **4**, 6032 (2010).
[9] A. Yella, H. W. Lee, H. N. Tsao, C. Yi, A. K. Chandiran, M. K. Nazeeruddin, E. W. Diau, C. Y. Yeh, S. M. Zakeeruddin, and M. Graützel, Science **334**, 629 (2011).
[10] M. Grätzel, Inorg. Chem. **44**, 6841 (2005).
[11] S. E. Koops, P. R. F. Barnes, B. C. O'Regan, and J. R. Durrant, J. Phys. Chem. C **114**, 8054 (2010).
[12] T. Marinado, K. Nonomura, J. Nissfolk, M. K. Karlsson, D. P. Hagberg, L. Sun, S. Mori, and A. Hagfeldt, Langmuir **26**, 2592 (2009).
[13] Z. Ning, Y. Fu, and H. Tian, Energy Environ. Sci. **3**, 1170 (2010).
[14] J. Bisquert, F. Fabregat-Santiago, and K. Kalyanasundaram, *Dye-sensitized Solar Cells* (CRC Press, Boca Raton, 2010).
[15] N. W. Duffy, L. M. Peter, and K. G. U. Wijayantha, Electrochem. Commun. **2**, 262 (2000).
[16] N. Kopidakis, K. D. Benkstein, J. van de Lagemaat, and A. J. Frank, J. Phys. Chem. B **107**, 11307 (2003).
[17] J. Nissfolk, K. Fredin, A. Hagfeldt, and G. Boschloo, J. Phys. Chem. B **110**, 17715 (2006).
[18] S. Nakade, T. Kanzaki, Y. Wada, and S. Yanagida, Langmuir **21**, 10803 (2005).
[19] J. Halme, P. Vahermaa, K. Miettunen, and P. Lund, Adv. Mater. **22**, E210 (2010).
[20] F. Fabregat-Santiago, G. Garcia-Belmonte, I. Mora-Sero, and J. Bisquert, Phys. Chem. Chem. Phys. **13**, 9083 (2011).
[21] L. Dloczik, O. Ileperuma, I. Lauermann, L. M. Peter, E. A. Ponomarev, G. Redmond, N. J. Shaw, and I. Uhlendorf, J. Phys. Chem. B **101**, 10281 (1997).
[22] R. Kern, R. Sastrawan, J. Ferber, R. Stangl, and J. Luther, Electrochim. Acta **47**, 4213 (2002).
[23] L. M. Peter, J. Phys. Chem. C **111**, 6601 (2007).
[24] A. Solbrand, H. Lindström, H. Rensmo, A. Hagfeldt, S.-E. Lindquist, and S. Södergren, J. Phys. Chem. B **101**, 2514 (1997).

[25] L. Luo, C.-J. Lin, C.-S. Hung, C.-F. Lo, C.-Y. Lin, and E. W.-G. Diau, Phys. Chem. Chem. Phys. **12**, 12973 (2010).

[26] Y.-C. Chang and E. W.-G. Diau. "Characterizations of Electron Transport and Charge Recombination Kinetics via Charge Extraction and Transient Photoelectric Methods" (unpublished).

[27] L. M. Peter, N. W. Duffy, R. L. Wang, and K. G. U. Wijayantha, J. Electroanal. Chem. **524**, 127 (2002).

[28] C. G. Shuttle, A. Maurano, R. Hamilton, B. O'Regan, J. C. de Mello, and J. R. Durrant, Appl. Phys. Lett. **93**, 183501 (2008).

[29] B. C. O'Regan, S. Scully, A. C. Mayer, E. Palomares, and J. Durrant, J. Phys. Chem. B **109**, 4616 (2005).

[30] Q. Wang, Z. Zhang, S. M. Zakeeruddin, and M. Graützel, J. Phys. Chem. C **112**, 7084 (2008).

[31] J. Halme, K. Miettunen, and P. Lund, J. Phys. Chem. C **112**, 20491 (2008).

[32] B. C. O'Regan, K. Bakker, J. Kroeze, H. Smit, P. Sommeling, and J. R. Durrant, J. Phys. Chem. B **110**, 17155 (2006).

[33] F. Fabregat-Santiago, J. Bisquert, G. Garcia-Belmonte, G. Boschloo, and A. Hagfeldt, Sol. Energy Mater. Sol. Cells **87**, 117 (2005).

[34] K. Zhu, S.-R. Jang, and A. J. Frank, J. Phys. Chem. Lett. **2**, 1070 (2011).

[35] R. Mohammadpour, A. Iraji zad, A. Hagfeldt, and G. Boschloo, Chemphyschem **11**, 2140 (2010).

[36] Z. Zhang, N. Evans, S. M. Zakeeruddin, R. Humphry-Baker, and M. Graützel, J. Phys. Chem. C **111**, 398 (2007).

[37] F. Gao, Y. Wang, D. Shi, J. Zhang, M. Wang, X. Jing, R. Humphry-Baker, P. Wang, S. M. Zakeeruddin, and M. Graützel, J. Am. Chem. Soc. **130**, 10720 (2008).

[38] A. Reynal, A. Forneli, E. Martinez-Ferrero, A. Sanchez-Diaz, A. Vidal-Ferran, B. C. O'Regan, and E. Palomares, J. Am. Chem. Soc. **130**, 13558 (2008).

[39] C. Y. Chen, N. Pootrakulchote, S. J. Wu, M. K. Wang, J. Y. Li, J. H. Tsai, C. G. Wu, S. M. Zakeeruddin, and M. Grätzel, J. Phys. Chem. C **113**, 20752 (2009).

[40] B. C. O'Regan, K. Walley, M. Juozapavicius, A. Anderson, F. Matar, T. Ghaddar, S. M. Zakeeruddin, C. Klein, and J. R. Durrant, J. Am. Chem. Soc. **131**, 3541 (2009).

[41] Q. Yu, S. Liu, M. Zhang, N. Cai, Y. Wang, and P. Wang, J. Phys. Chem. C **113**, 14559 (2009).

[42] W.-K. Huang, C.-W. Cheng, S.-M. Chang, Y.-P. Lee, and E. W.-G. Diau, Chem. Commun. **46**, 8992 (2010).

[43] X. Lv, F. Wang, and Y. Li, ACS Appl. Mater. Interfaces **2**, 1980 (2010).

[44] C.-Y. Chen, N. Pootrakulchote, T.-H. Hung, C.-J. Tan, H.-H. Tsai, S. M. Zakeeruddin, C.-G. Wu, and M. Grätzel, J. Phys. Chem. C **115**, 20043 (2011).

[45] A. Mishra, N. Pootrakulchote, M. Wang, S.-J. Moon, S. M. Zakeeruddin, M. Grätzel, and P. Bäuerle, Adv. Funct. Mater. **21**, 963 (2011).

[46] N. Koumura, Z. S. Wang, S. Mori, M. Miyashita, E. Suzuki, and K. Hara, J. Am. Chem. Soc. **128**, 14256 (2006).

[47] W. H. Howie, F. Claeyssens, H. Miura, and L. M. Peter, J. Am. Chem. Soc. **130**, 1367 (2008).

[48] M. Miyashita, K. Sunahara, T. Nishikawa, Y. Uemura, N. Koumura, K. Hara, A. Mori, T. Abe, E. Suzuki, and S. Mori, J. Am. Chem. Soc. **130**, 17874 (2008).

[49] D. Shi, Y. M. Cao, N. Pootrakulchote, Z. H. Yi, M. F. Xu, S. M. Zakeeruddin, M. Graetzel, and P. Wang, J. Phys. Chem. C **112**, 17478 (2008).

[50] M. Wang, M. Xu, D. Shi, R. Li, F. Gao, G. Zhang, Z. Yi, R. Humphry-Baker, P. Wang, S. M. Zakeeruddin, and M. Grätzel, Adv. Mater. **20**, 4460 (2008).

[51] M. Xu, R. Li, N. Pootrakulchote, D. Shi, J. Guo, Z. Yi, S. M. Zakeeruddin, M. Graützel, and P. Wang, J. Phys. Chem. C **112**, 19770 (2008).

[52] J. H. Yum, S. J. Moon, R. Humphry-Baker, P. Walter, T. Geiger, F. Nuesch, M. Graützel, and M. D. Nazeeruddin, Nanotechnology **19**, 424005 (2008).

Downloaded by [National Chiao Tung University] at 06:29 21 November 2012

[53] N. Koumura, Z.-S. Wang, M. Miyashita, Y. Uemura, H. Sekiguchi, Y. Cui, A. Mori, S. Mori, and K. Hara, J. Mater. Chem. **19**, 4829 (2009).
[54] R. Li, X. Lv, D. Shi, D. Zhou, Y. Cheng, G. Zhang, and P. Wang, J. Phys. Chem. C **113**, 7469 (2009).
[55] S.-J. Moon, J.-H. Yum, R. Humphry-Baker, K. M. Karlsson, D. P. Hagberg, T. Marinado, A. Hagfeldt, L. Sun, M. Graützel, and M. K. Nazeeruddin, J. Phys. Chem. C **113**, 16816 (2009).
[56] M. Xu, S. Wenger, H. Bala, D. Shi, R. Li, Y. Zhou, S. M. Zakeeruddin, M. Graützel, and P. Wang, J. Phys. Chem. C **113**, 2966 (2009).
[57] S. M. Feldt, E. A. Gibson, E. Gabrielsson, L. Sun, G. Boschloo, and A. Hagfeldt, J. Am. Chem. Soc. **132**, 16714 (2010).
[58] M. K. R. Fischer, S. Wenger, M. Wang, A. Mishra, S. M. Zakeeruddin, M. Graützel, and P. Baüuerle, Chem. Mater. **22**, 1836 (2010).
[59] X. Jiang, T. Marinado, E. Gabrielsson, D. P. Hagberg, L. Sun, and A. Hagfeldt, J. Phys. Chem. C **114**, 2799 (2010).
[60] R. Li, J. Liu, N. Cai, M. Zhang, and P. Wang, J. Phys. Chem. B **114**, 4461 (2010).
[61] S. Wenger, P.-A. Bouit, Q. Chen, J. l. Teuscher, D. D. Censo, R. Humphry-Baker, J.-E. Moser, J. L. Delgado, N. Martín, S. M. Zakeeruddin, and M. Graützel, J. Am. Chem. Soc. **132**, 5164 (2010).
[62] W. Zeng, Y. Cao, Y. Bai, Y. Wang, Y. Shi, M. Zhang, F. Wang, C. Pan, and P. Wang, Chem. Mater. **22**, 1915 (2010).
[63] L. Alibabaei, M. Wang, R. Giovannetti, J. Teuscher, D. Di Censo, J.-E. Moser, P. Comte, F. Pucciarelli, S. M. Zakeeruddin, and M. Grätzel, Energy Environ. Sci. **3**, 956 (2010).
[64] Y. C. Chang, C. L. Wang, T. Y. Pan, S. H. Hong, C. M. Lan, H. H. Kuo, C. F. Lo, H. Y. Hsu, C. Y. Lin, and E. W. Diau, Chem. Commun. **47**, 8910 (2011).
[65] K.-S. Ahn, M.-S. Kang, J.-K. Lee, B.-C. Shin, and J.-W. Lee, Appl. Phys. Lett. **89**, 013103 (2006).
[66] A. K. Chandiran, F. d. r. Sauvage, M. Casas-Cabanas, P. Comte, S. M. Zakeeruddin, and M. Graetzel, J. Phys. Chem. C **114**, 15849 (2010).
[67] X. Wang, S. Karanjit, L. Zhang, H. Fong, Q. Qiao, and Z. Zhu, Appl. Phys. Lett. **98**, 082114 (2011).
[68] G. Tsekouras, M. Miyashita, K. Yung Kent, T. Wey Yang, A. J. Mozer, R. Amal, S. Mori, and G. G. Wallace, IEEE J. Set. Top. Quant. **16**, 1641 (2010).
[69] S. Nakade, T. Kanzaki, W. Kubo, T. Kitamura, Y. Wada, and S. Yanagida, J. Phys. Chem. B **109**, 3480 (2005).
[70] Y. Bai, Y. Cao, J. Zhang, M. Wang, R. Li, P. Wang, S. M. Zakeeruddin, and M. Graützel, Nat. mater. **7**, 626 (2008).
[71] Y. Cao, J. Zhang, Y. Bai, R. Li, S. M. Zakeeruddin, M. Graützel, and P. Wang, J. Phys. Chem. C **112**, 13775 (2008).
[72] C. Xi, Y. Cao, Y. Cheng, M. Wang, X. Jing, S. M. Zakeeruddin, M. Graützel, and P. Wang, J. Phys. Chem. C **112**, 11063 (2008).
[73] Z. Zhang, P. Chen, T. N. Murakami, S. M. Zakeeruddin, and M. Grätzel, Adv. Funct. Mater. **18**, 341 (2008).
[74] N. Cai, J. Zhang, D. Zhou, Z. Yi, J. Guo, and P. Wang, J. Phys. Chem. C **113**, 4215 (2009).
[75] Z.-S. Wang, N. Koumura, Y. Cui, M. Miyashita, S. Mori, and K. Hara, Chem. Mater. **21**, 2810 (2009).
[76] M. Wang, N. Chamberland, L. Breau, J. E. Moser, R. Humphry-Baker, B. Marsan, S. M. Zakeeruddin, and M. Graützel, Nat. Chem. **2**, 385 (2010).
[77] Y.-C. Chang, W.-K. Huang and E. W.-G. Diau. "Understanding Electron Transport and Charge Recombination Kinetics for Heteroleptic Ruthenium Sensitizers in Dye-sensitized Solar Cells" (unpublished).

Downloaded by [National Chiao Tung University] at 06:29 21 November 2012

Downloaded by [National Chiao Tung University] at 06:29 21 November 2012

[78] J.-W. Shiu, C.-M. Lan, Y.-C. Chang, and E. W.-G. Diau. ‘‘Size-controlled Anatase Titania Single Crystals with Octahedron-like Morphology for Dye-sensitized Solar Cells’’ (unpublished).

[79] Y.-C. Chang, J.-W. Shiu and E. W.-G. Diau. ‘‘Understanding Electron Transport and Charge Recombination Kinetics for Dye-sensitized Solar Cells: Conventional Titania Nanoparticles vs. Octahedral Single Crystals’’ (unpublished).

[80] H. Imahori, T. Umeyama, and S. Ito, Acc. Chem. Res. **42**, 1809 (2009).

[81] M. V. Martinez-Diaz, G. de la Torre, and T. Torres, Chem. Commun. **46**, 7090 (2010).

[82] C.-W. Lee, H.-P. Lu, C.-M. Lan, Y.-L. Huang, Y.-R. Liang, W.-N. Yen, Y.-C. Liu, Y.-S. Lin, E. W.-G. Diau, and C.-Y. Yeh, Chem. Eur. J. **15**, 1403 (2009).

[83] H.-P. Lu, C.-L. Mai, C.-Y. Tsia, S.-J. Hsu, C.-P. Hsieh, C.-L. Chiu, C.-Y. Yeh, and E. W.-G. Diau, Phys. Chem. Chem. Phys. **11**, 10270 (2009).

[84] H.-P. Lu, C.-Y. Tsai, W.-N. Yen, C.-P. Hsieh, C.-W. Lee, C.-Y. Yeh, and E. W.-G. Diau, J. Phys. Chem. C **113**, 20990 (2009).

[85] C.-P. Hsieh, H.-P. Lu, C.-L. Chiu, C.-W. Lee, S.-H. Chuang, C.-L. Mai, W.-N. Yen, S.-J. Hsu, E. W.-G. Diau, and C.-Y. Yeh, J. Mater. Chem. **20**, 1127 (2010).

[86] T. Bessho, S. M. Zakeeruddin, C.-Y. Yeh, E. W.-G. Diau, and M. Grätzel, Angew. Chem. Int. Ed. **49**, 6646 (2010).

[87] C.-Y. Lin, C.-F. Lo, L. Luo, H.-P. Lu, C.-S. Hung, and E. W.-G. Diau, J. Phys. Chem. C **113**, 755 (2008).

[88] C.-Y. Lin, Y.-C. Wang, S.-J. Hsu, C.-F. Lo, and E. W.-G. Diau, J. Phys. Chem. C **114**, 687 (2009).

[89] C.-F. Lo, S.-J. Hsu, C.-L. Wang, Y.-H. Cheng, H.-P. Lu, E. W.-G. Diau, and C.-Y. Lin, J. Phys. Chem. C **114**, 12018 (2010).

[90] C.-L. Wang, Y.-C. Chang, C.-M. Lan, C.-F. Lo, E. Wei-Guang Diau, and C.-Y. Lin, Energy Environ. Sci. **4**, 1788 (2011).

[91] C.-L. Wang, C.-M. Lan, S.-H. Hong, Y.-F. Wang, T.-Y. Pan, C.-W. Chang, H.-H. Kuo, M.-Y. Kuo, E. W.-G. Diau, and C.-Y. Lin, Energy Environ. Sci. **5**, 6933 (2012).

[92] D. P. Hagberg, J.-H. Yum, H. Lee, F. De Angelis, T. Marinado, K. M. Karlsson, R. Humphry-Baker, L. Sun, A. Hagfeldt, M. Grätzel, and M. K. Nazeeruddin, J. Am. Chem. Soc. **130**, 6259 (2008).

[93] A. J. Mozer, P. Wagner, D. L. Officer, G. G. Wallace, W. M. Campbell, M. Miyashita, K. Sunahara, and S. Mori, Chem. Commun. **39**, 4741 (2008).

[94] M. Pavanello, L. Adamowicz, M. Volobuyev, and B. Mennucci, J. Phys. Chem. B **114**, 4416 (2010).

[95] P. Wang, S. M. Zakeeruddin, J. E. Moser, M. K. Nazeeruddin, T. Sekiguchi, and M. Graützel, Nat. Mater. **2**, 402 (2003).

[96] P. Wang, S. M. Zakeeruddin, P. Comte, R. Charvet, R. Humphry-Baker, and M. Grätzel, J. Phys. Chem. B **107**, 14336 (2003).

[97] W.-K. Huang, H.-P. Wu, P.-L. Lin, Y.-P. Lee, and E. W.-G. Diau, J. Phys. Chem. Lett. **3**, 1830 (2012).

[98] S. Ito, P. Chen, P. Comte, M. K. Nazeeruddin, P. Liska, P. Péchy, and M. Grätzel, Prog. Photovoltaics **15**, 603 (2007).

[99] S. Nakade, Y. Saito, W. Kubo, T. Kitamura, Y. Wada, and S. Yanagida, J. Phys. Chem. B **107**, 8607 (2003).

[100] M. E. Orazem and B. Tribollet, *Electrochemical Impedance Spectroscopy* (John Wiley & Sons, Inc., New Jersey, 2008).

[101] Q. Wang, S. Ito, M. Grätzel, F. Fabregat-Santiago, I. Mora-Sero, J. Bisquert, T. Bessho, and H. Imai, J. Phys. Chem. B **110**, 25210 (2006).

[102] M. Wang, P. Chen, R. Humphry-Baker, S. M. Zakeeruddin, and M. Grätzel, Chemphyschem **10**, 290 (2009).

[103] J. Bisquert, J. Electroanal. Chem. **646**, 43 (2010).
[104] J. Bisquert, J. Phys. Chem. B **106**, 325 (2002).
[105] J. Bisquert, Phys. Chem. Chem. Phys. **10**, 49 (2008).
[106] G. Schlichthorl, S. Y. Huang, J. Sprague, and A. J. Frank, J. Phys. Chem. B **101**, 8141 (1997).
[107] F. Fabregat-Santiago, J. Bisquert, E. Palomares, L. Otero, D. B. Kuang, S. M. Zakeeruddin, and M. Graützel, J. Phys. Chem. C **111**, 6550 (2007).
[108] J. Bisquert and I. Mora-Sero, J. Phys. Chem. Lett. **1**, 450 (2010).
[109] J. Villanueva-Cab, G. Oskam, and J. A. Anta, Sol. Energy Mater. Sol. Cells **94**, 45 (2010).
[110] J. Halme, Phys. Chem. Chem. Phys. **13**, 12435 (2011).
[111] CIMPS program user manual, Zahner.
[112] A. J. Bard and L. R. Faulkner, *Electrochemical Methods—Fundamentals and Applications*, 2nd ed. (John Wiley & Sons, New York, 2001).
[113] E. Barsoukov and J. R. Macdonald, *Impedance Spectroscopy: Theory, Experiment, and Applications*, 2nd ed. (John Wiley & Sons, New Jersey, 2005).
[114] J. Bisquert, G. Garcia-Belmonte, F. Fabregat-Santiago, N. S. Ferriols, P. Bogdanoff, and E. C. Pereira, J. Phys. Chem. B **104**, 2287 (2000).
[115] A. Pitarch, G. Garcia-Belmonte, I. Mora-Sero, and J. Bisquert, Phys. Chem. Chem. Phys. **6**, 2983 (2004).
[116] http://www.scribner.com
[117] M. Adachi, M. Sakamoto, J. T. Jiu, Y. Ogata, and S. Isoda, J. Phys. Chem. B **110**, 13872 (2006).
[118] Z. P. Huo, S. Y. Dai, C. G. Zhang, F. T. Kong, X. Q. Fang, L. Guo, W. Q. Liu, L. H. Hu, X. Pan, and K. J. Wang, J. Phys. Chem. B **112**, 12927 (2008).
[119] D. Kuang, S. Uchida, R. Humphry-Baker, S. M. Zakeeruddin, and M. Grätzel, Angew. Chem. Int. Ed. **47**, 1923 (2008).
[120] Z.-S. Wang, N. Koumura, Y. Cui, M. Takahashi, H. Sekiguchi, A. Mori, T. Kubo, A. Furube, and K. Hara, Chem. Mater. **20**, 3993 (2008).
[121] K. Hara, K. Miyamoto, Y. Abe, and M. Yanagida, J. Phys. Chem. B **109**, 23776 (2005).
[122] M. Yanagida, K. Sayama, K. Kasuga, M. Kurashige, and H. Sugihara, J. Photochem. Photobiol., A **182**, 288 (2006).
[123] M. Yanagida, K. Miyamoto, K. Sayama, K. Kasuga, M. Kurashige, Y. Abe, and H. Sugihara, J. Phys. Chem. C **111**, 201 (2007).
[124] S. S. Pandey, T. Inoue, N. Fujikawa, Y. Yamaguchi, and S. Hayase, J. Photochem. Photobiol., A **214**, 269 (2010).
[125] Y. Cui, Y. Wu, X. Lu, X. Zhang, G. Zhou, F. B. Miapeh, W. Zhu, and Z.-S. Wang, Chem. Mater. **23**, 4394 (2011).
[126] H. Paulsson, L. Kloo, A. Hagfeldt, and G. Boschloo, J. Electroanal. Chem. **586**, 56 (2006).
[127] W. Q. Liu, D. X. Kou, M. L. Cai, L. H. Hu, J. Sheng, H. J. Tian, N. Q. Jiang, and S. Y. Dai, J. Phys. Chem. C **114**, 9965 (2010).
[128] F. Hao, H. Lin, Y. Liu, and J. Li, Electrochem. Commun. **13**, 550 (2011).
[129] F. Hao, H. Lin, Y. Liu, G. Yang, G. Wang, and J. Li, Electrochim. Acta **56**, 5605 (2011).
[130] R. Gao, L. Wang, Y. Geng, B. Ma, Y. Zhu, H. Dong, and Y. Qiu, J. Phys. Chem. C **115**, 17986 (2011).
[131] M. Wang, X. Pan, X. Fang, L. Guo, C. Zhang, Y. Huang, Z. Huo, and S. Dai, J. Power Sources **196**, 5784 (2011).
[132] H. Geng, R. Peng, S. Han, X. Gu, and M. Wang, J. Electron. Mater. **39**, 2346 (2010).
[133] H. Geng, Y. Guo, R. Peng, S. Han, and M. Wang, Sol. Energy Mater. Sol. Cells **94**, 1293 (2010).
[134] S. R. Jang, K. Zhu, M. J. Ko, K. Kim, C. Kim, N. G. Park, and A. J. Frank, ACS Nano **5**, 8267 (2011).

Downloaded by [National Chiao Tung University] at 06:29 21 November 2012

[135] D. Zhang, T. Yoshida, T. Oekermann, K. Furuta, and H. Minoura, Adv. Funct. Mater. **16**, 1228 (2006).

[136] M. Yanagida, K. Miyamoto, K. Sayama, K. Kasuga, M. Kurashige, S. Takano, G. Fujihashi, Y. Abe, and H. Sugihara, Electrochim. Acta **51**, 3993 (2006).

[137] S. M. Waita, B. O. Aduda, J. M. Mwabora, C. G. Granqvist, S.-E. Lindquist, G. A. Niklasson, A. Hagfeldt, and G. Boschloo, J. Electroanal. Chem. **605**, 151 (2007).

[138] K. Pan, Y. Dong, C. Tian, W. Zhou, G. Tian, B. Zhao, and H. Fu, Electrochim. Acta **54**, 7350 (2009).

[139] K. Kim, G.-W. Lee, K. Yoo, D. Y. Kim, J.-K. Kim, and N.-G. Park, J. Photochem. Photobiol., A **204**, 144 (2009).

[140] W. Liu, L. Hu, S. Dai, L. Guo, N. Jiang, and D. Kou, Electrochim. Acta **55**, 2338 (2010).

[141] H. Geng, Q. Qu, C. Chen, H. Wu, and M. Wang, J. Electron. Mater. **39**, 1 (2009).

[142] P.-T. Hsiao, Y.-L. Tung, and H. Teng, J. Phys. Chem. C **114**, 6762 (2010).

[143] J. Sheng, L. Hu, W. Li, L. e. Mo, H. Tian, and S. Dai, Sol. Energy **85**, 2697 (2011).

[144] E. Enache-Pommer, J. E. Boercker, and E. S. Aydil, Appl. Phys. Lett. **91**, 123116 (2007).

[145] K. Zhu, N. R. Neale, A. Miedaner, and A. J. Frank, Nano Lett **7**, 69 (2007).

[146] J. Qu, X. P. Gao, G. R. Li, Q. W. Jiang, and T. Y. Yan, J. Phys. Chem. C **113**, 3359 (2009).

[147] E. Enache-Pommer, B. Liu, and E. S. Aydil, Phys. Chem. Chem. Phys. **11**, 9648 (2009).

[148] K. P. Wang and H. Teng, Phys. Chem. Chem. Phys. **11**, 9489 (2009).

[149] W. Guo, L. Wu, Z. Chen, G. Boschloo, A. Hagfeldt, and T. Ma, J. Photochem. Photobiol., A **219**, 180 (2011).

[150] C. Zhang, S. Chen, L. e. Mo, Y. Huang, H. Tian, L. Hu, Z. Huo, S. Dai, F. Kong, and X. Pan, J. Phys. Chem. C **115**, 16418 (2011).

[151] X. Zhang, F. Liu, Q.-L. Huang, G. Zhou, and Z.-S. Wang, J. Phys. Chem. C **115**, 12665 (2011).

[152] T. Oekermann, T. Yoshida, H. Minoura, K. G. U. Wijayantha, and L. M. Peter, J. Phys. Chem. B **108**, 8364 (2004).

[153] M. Quintana, T. Edvinsson, A. Hagfeldt, and G. Boschloo, J. Phys. Chem. C **111**, 1035 (2007).

[154] D. Bi, F. Wu, W. Yue, Y. Guo, W. Shen, R. Peng, H. Wu, X. Wang, and M. Wang, J. Phys. Chem. C **114**, 13846 (2010).

[155] L.-L. Li, Y.-J. Chen, H.-P. Wu, N. S. Wang, and E. W.-G. Diau, Energy Environ. Sci. **4**, 3420 (2011).

[156] T. Ripolles-Sanchis, B.-C. Guo, H.-P. Wu, T.-Y. Pan, H.-W. Lee, S. R. Raga, F. Fabregat-Santiago, J. Bisquert, C.-Y. Yeh, and E. W.-G. Diau, Chem. Commun. **48**, 4368 (2012).

[157] C.-M. Lan, H.-P. Wu, T.-Y. Pan, C.-W. Chang, W.-S. Chao, C.-T. Chen, C.-L. Wang, C.-Y. Lin, and E. W.-G. Diau, Energy Environ. Sci. **5**, 6460 (2012).

[158] H.-P. Wu J.-W. Shiu and E. W.-G. Diau. "Characterizations of Electron Transport and Charge Recombination Kinetics via Charge Extraction and Impedance Spectroscopy Methods" (unpublished).

[159] L. Andrade, S. M. Zakeeruddin, M. K. Nazeeruddin, H. A. Ribeiro, A. Mendes, and M. Grätzel, Chemphyschem **10**, 1117 (2009).

[160] J. J. Wu, G. R. Chen, C. C. Lu, W. T. Wu, and J. S. Chen, Nanotechnology **19**, 105702 (2008).

[161] X. Pan, S.-Y. Dai, K.-J. Wang, L.-H. Hu, C.-W. Shi, L. Guo, and F.-T. Kong, Chin. J. Chem. **23**, 1579 (2005).

[162] D. Kuang, J. Brillet, P. Chen, M. Takata, S. Uchida, H. Miura, K. Sumioka, S. M. Zakeeruddin, and M. Grätzel, ACS Nano **2**, 1113 (2008).

[163] X. Lü, X. Mou, J. Wu, D. Zhang, L. Zhang, F. Huang, F. Xu, and S. Huang, Adv. Funct. Mater. **20**, 509 (2010).

[164] C. Grimes and G. K. Mor, *TiO_2 Nanotube Arrays: Synthesis, Properties, and Applications* (Springer Verlag, New York, 2009).

[165] O. K. Varghese, M. Paulose, and C. A. Grimes, Nat. Nanotech. **4**, 592 (2009).

[166] J. H. Park, T.-W. Lee, and M. G. Kang, Chem. Commun. **25**, 2867 (2008).

Downloaded by [National Chiao Tung University] at 06:29 21 November 2012

Downloaded by [National Chiao Tung University] at 06:29 21 November 2012

[167] C. Xu, P. H. Shin, L. Cao, J. Wu, and D. Gao, Chem. Mater. **22**, 143 (2009).

[168] D. Kuang, P. Comte, S. M. Zakeeruddin, D. P. Hagberg, K. M. Karlsson, L. Sun, M. K. Nazeeruddin, and M. Grätzel, Sol. Energy **85**, 1189 (2011).

[169] J. Liu, R. Li, X. Si, D. Zhou, Y. Shi, Y. Wang, X. Jing, and P. Wang, Energy Environ. Sci. **3**, 1924 (2010).

[170] M. A. Hossain, J. R. Jennings, Z. Y. Koh, and Q. Wang, ACS Nano **5**, 3172 (2011).

[171] Y. Liu, J. R. Jennings, Y. Huang, Q. Wang, S. M. Zakeeruddin, and M. Graützel, J. Phys. Chem. C **115**, 18847 (2011).

[172] D. Zhou, Q. Yu, N. Cai, Y. Bai, Y. Wang, and P. Wang, Energy Environ. Sci. **4**, 2030 (2011).

[173] J. R. Jennings, Y. Liu, F. Safari-Alamuti, and Q. Wang, J. Phys. Chem. C **116**, 1556 (2012).

[174] B. E. Hardin, A. Sellinger, T. Moehl, R. Humphry-Baker, J. E. Moser, P. Wang, S. M. Zakeeruddin, M. Graützel, and M. D. McGehee, J. Am. Chem. Soc. **133**, 10662 (2011).

[175] X. Z. Liu, W. Zhang, S. Uchida, L. P. Cai, B. Liu, and S. Ramakrishna, Adv. Mater. **22**, E150 (2010).

[176] M. Wang, C. Grätzel, S.-J. Moon, R. Humphry-Baker, N. Rossier-Iten, S. M. Zakeeruddin, and M. Grätzel, Adv. Funct. Mater. **19**, 2163 (2009).

[177] S. M. Zakeeruddin and M. Grätzel, Adv. Funct. Mater. **19**, 2187 (2009).

[178] K. Mukherjee, T.-H. Teng, R. Jose, and S. Ramakrishna, Appl. Phys. Lett. **95**, 012101 (2009).

[179] A. B. F. Martinson, M. S. Goes, F. Fabregat-Santiago, J. Bisquert, M. J. Pellin, and J. T. Hupp, J. Phys. Chem. A **113**, 4015 (2009).

[180] C. He, Z. Zheng, H. L. Tang, L. N. Zhao, and F. Lu, J. Phys. Chem. C **113**, 10322 (2009).

[181] F. Sauvage, F. Di Fonzo, A. Li Bassi, C. S. Casari, V. Russo, G. Divitini, C. Ducati, C. E. Bottani, P. Comte, and M. Graützel, Nano Lett **10**, 2562 (2010).

[182] E. M. Barea, C. Zafer, B. Gultekin, B. Aydin, S. Koyuncu, S. Icli, F. F. Santiago, and J. Bisquert, J. Phys. Chem. C **114**, 19840 (2010).

[183] E. M. Barea, V. Goínzalez-Pedro, T. Ripolleís-Sanchis, H.-P. Wu, L.-L. Li, C.-Y. Yeh, E. W.-G. Diau, and J. Bisquert, J. Phys. Chem. C **115**, 10898 (2011).

[184] E. M. Barea, J. Ortiz, F. J. Payá, F. Fernández-Lázaro, F. Fabregat-Santiago, A. Sastre-Santos, and J. Bisquert, Energy Environ. Sci. **3**, 1985 (2010).

[185] P. Sudhagar, T. Song, D. H. Lee, I. n. Mora-Seroí, J. Bisquert, M. Laudenslager, W. M. Sigmund, W. I. Park, U. Paik, and Y. S. Kang, J. Phys. Chem. Lett. **2**, 1984 (2011).

[186] M. Samadpour, P. P. Boix, S. Gimeínez, A. Iraji Zad, N. Taghavinia, I. n. Mora-Seroí, and J. Bisquert, J. Phys. Chem. C **115**, 14400 (2011).

[187] E. M. Barea, M. Shalom, S. Gimenez, I. Hod, I. Mora-Sero, A. Zaban, and J. Bisquert, J. Am. Chem. Soc. **132**, 6834 (2010).

[188] F. Fabregat-Santiago, J. Bisquert, E. Palomares, S. A. Haque, and J. R. Durrant, J. Appl. Phys. **100**, 034510 (2006).

[189] E. Barea, X. Xu, V. González-Pedro, T. Ripollés-Sanchis, F. Fabregat-Santiago, and J. Bisquert, Energy Environ. Sci. **4**, 3414 (2011).

[190] A. S. Gonçalves, M. S. Góes, F. Fabregat-Santiago, T. Moehl, M. R. Davolos, J. Bisquert, S. Yanagida, A. F. Nogueira, and P. R. Bueno, Electrochim. Acta **56**, 6503 (2011).

[191] T. C. Li, M. S. Goes, F. Fabregat-Santiago, J. Bisquert, P. R. Bueno, C. Prasittichai, J. T. Hupp, and T. J. Marks, J. Phys. Chem. C **113**, 18385 (2009).

[192] B.-S. Chen, D.-Y. Chen, C.-L. Chen, C.-W. Hsu, H.-C. Hsu, K.-L. Wu, S.-H. Liu, P.-T. Chou, and Y. Chi, J. Mater. Chem. **21**, 1937 (2011).

[193] W.-S. Chao, K.-H. Liao, C.-T. Chen, W.-K. Huang, C.-M. Lan, and E. W.-G. Diau, Chem. Commun. **48**, 4884 (2012).

[194] L. Han, A. Islam, H. Chen, C. Malapaka, B. Chiranjeevi, S. Zhang, X. Yang, and M. Yanagida, Energy Environ. Sci. **5**, 6057 (2012).

[195] J. N. Clifford, A. Forneli, H. Chen, T. Torres, S. Tan, and E. Palomares, J. Mater. Chem. **21**, 1693 (2011).